Fall 2015

Methods for checking and enforcing physical quality of linear electrical network models

Mikhail Zvonkin

Department:

METHODS FOR CHECKING AND ENFORCING PHYSICAL QUALITY OF LINEAR ELECTRICAL NETWORK MODELS

by

MIKHAIL ZVONKIN

A THESIS

Presented to the Faculty of the Graduate School of the

MISSOURI UNIVERSITY OF SCIENCE AND TECHNOLOGY

In Partial Fulfillment of the Requirements for the Degree

MASTER OF SCIENCE IN ELECTRICAL ENGINEERING

2015

Approved by

Dr. James L. Drewniak, Advisor
Dr. Mikheil Tsiklauri, Co-advisor
Dr. Jun Fan

ABSTRACT

Most CAD tools allow system-level simulation for signal integrity by computing and connecting models together for the various sub-parts. The success of this model derivation depends on the quality of the network parameters. Different errors may seriously affect the quality of the frequency characterization: frequency-dependent measurement errors, errors due to the numerical simulation and/or discretization, etc. When these errors are large, model assembly and simulation becomes difficult and may even fail. This thesis gives an overview of the most significant properties of physically valid network parameters, describes existing methods for checking and enforcing these properties, and presents several new methodologies for checking and enforcing causality. A time domain methodology based on the vector fitting approximation as well as the frequency domain methodologies based on the Kramers-Kronig relations enforcement by numerical integration and Fast Fourier Transform are presented. A new algorithm is developed for a stable recursive convolution after time domain causality enforcement. In addition, global qualities of data for system simulations are discussed: a study of an accurate causal frequency domain interpolation as well as a robust technique for extrapolation to DC is included.

ACKNOWLEDGMENTS

I would like to thank everyone who helped and supported me through these three years of graduate school at the EMC Laboratory of Missouri University of Science and Technology in Rolla. First and foremost, I would like to thank my academic advisors Dr. James L. Drewniak and Dr. Mikheil Tsiklauri for all their guidance through this time.

Dr. James Drewniak has been an exceptional example of leadership, professionalism, and work ethics. His dedication to the success of the EMC laboratory and each and every one of his students is admirable and inspiring.

I cannot fully describe how lucky I was to be able to work with Dr. Mikheil Tsiklauri. His creativity, responsiveness, ability to listen to others, and lead the team with everlasting optimism is a source of inspiration and a major part of my success. I would like to thank him for the wonderful opportunity of partnership in research, work and everyday life.

Also, I would like to thank Dr. Marina Koledintseva for presenting me with the opportunity to become a graduate student here. I am very grateful to her for assisting me when I arrived and since.

My research here would not be possible without all the amazing professors who provided me with insightful discussions and shared their knowledge. I would like to specifically thank Dr. Jun Fan and Dr. Nana Dikhaminjia.

Last, I would like to thank my family and friends for supporting me every step of the way from all around the world: my mom, dad, and my sister ,Olga, who are always by my side; my friends from Russia Mikhail Seryakov, Evgenia Kuznetsova, Stas Makeev, and Desislava Makeeva who stay connected over the distance; and of course the amazing people that I met in Rolla and hope to stay close with for the rest of my life: Alyssa De Santi, Giorgi Maghlakelidze, Ketan Shringarpure, and Mikheil Tsiklauri.

This thesis is based on upon work supported partially by National Science Foundation under Grant No. IIP-1440110.

TABLE OF CONTENTS

Page

LIST OF ILLUSTRATIONS

Page

LIST OF TABLES

Page

1. QUALITY PROPERTIES OF ELECTRICAL LINEAR NETWORKS

1.1. LINEAR NETWORK MODEL OF A PHYSICAL SYSTEMS

As modern industry standards reach higher speeds and more complicated electrical interfaces are used, the role of signal integrity analysis increasingly grows. Electrical signals have to travel between I/O through packages, connectors, traces, and vias of the printed circuit boards, backplanes, and more. The goal of signal integrity analysis is to provide an accurate assessment of electrical link-paths, connecting a set of transmitting and receiving devices to estimate the reliability of the link for signal propagation. The complexity of such systems and numerous factors affecting the signal naturally leads to the need of a mathematical model to describe this system that can be both analyzed and used as a foundation for computer simulations. Linear electrical networks are widely used to model such systems. However, mathematical modeling is also a source of inaccuracies due to assumptions and approximations, as well as the imperfections in the data that the model is applied to. Very thorough and careful handling of the model construction and data modification and validation is necessary for the trustworthy results and conclusions. This section provides a brief overview of this well-known model and introduces concepts and definitions necessary for the rest of this work.

1.1.1. Brief Overview of a Linear Network Modeling Approach. A linear electrical system is defined as a set of ports, where each port may have an input signal $u_i(t)$ and an output signal $v_j^{u_i}(t)$, a response of $u_i(t)$ observed at port j. Typically, a time signal represents voltage amplitude measured at the corresponding electrical port. One of the key assumptions of this model is linearity, which means the response of a linear combination of signals is a linear combination of responses. Formally:

$$v_k^{au_i+bu_j}(t) = av_k^{u_i}(t) + bv_k^{u_j}(t). \quad (1)$$

Linearity makes it possible to define a total response at a port $v_k(t)$:

$$v_k(t) = v_k^{\sum_{i=1}^{N} u_i(t)}(t) = \sum_{i=1}^{N} v_k^{u_i(t)}(t). \quad (2)$$

Another important property of the model is time invariance. This property means that there is no dependence on the time the input signal was injected: if the input signal is shifted in time, the output signal, the channel response, is shifted in time by the same amount. Formally:

$$v_k^{u_i(t+\tau)}(t) = v_k^{u_i(t)}(t+\tau). \quad (3)$$

Each pair of ports defines a channel. Linearity provides a convenient way to characterize each channel individually. The following section describes network characterization parameters and functions.

1.1.2. Impulse Response, Transfer Function, and Network Parameters. Any linear, time invariant system can be characterized by an impulse response [1]. Impulse response $h(t)$ is a response of a system to a Dirac delta function. For a given system:

$$v^{u(t)}(t) = h(t) * u(t), \quad (4)$$

where "$*$" denotes convolution. Further, the Fourier transform of a square-integrable time domain function $r(t)$ is defined as [2]:

$$\mathbb{F}\{r(t)\} = R(\omega) = \int_{-\infty}^{\infty} r(t)e^{-j\omega t}dt. \quad (5)$$

This representation is called frequency domain representation. Using the convolution theorem [2] it can be shown that the time domain formula (4) is equivalent to the following frequency domain formula:

$$V(\omega) = H(\omega) \cdot U(\omega), \tag{6}$$

where $H(\omega) = \mathbb{F}\{h(t)\}$ is called the transfer function of the system. Therefore, each channel of a linear electrical network can be characterized by the impulse response in the time domain and transfer function in the frequency domain.

There are several commonly used frequency domain parameters that comprehensively define a specific network. One of the most used types of parameters is scattering parameters or S-parameters [3]. An S-parameter is a frequency dependent matrix with the following definition of its elements:

$$S_{ji}(\omega) = \frac{V_j(\omega)}{V_i(\omega)}, \tag{7}$$

where $V_i(\omega)$ is a frequency domain representation of an input signal at the port i and $V_j(\omega)$ is a frequency domain response at the port j, assuming that there are no other input signals in the system besides $V_i(\omega)$. The transfer function matrix that contains frequency-dependent relations between input and output ports can be derived from the S-parameter matrix, taking into account the port impedances matrix and the reference impedance of the network [3]. The following formula relates the transfer function and S-parameters:

$$H(\omega) = \frac{\sqrt{Z_0}(Z_{out} + I)(I - S_{22}Z_{out})^{-1}S_{21}}{\left(\sqrt{Z_0}I + \frac{1}{\sqrt{Z_0}}Z_{in}\right) + \left(\sqrt{Z_0}I - \frac{1}{\sqrt{Z_0}}Z_{in}\right)(S_{11} + S_{12}Z_{out}(I - S_{22}Z_{out})^{-1}S_{21}} \tag{8}$$

where Z_0 is a reference impedance, Z_{in} is a matrix of input port impedances, Z_{out} is a matrix of output port impedances, I is an identity matrix and the S-parameter matrix is split into four submatrices: S_{11} relates input ports to input ports, S_{12} relates

input ports to output ports, S_{21} relates output ports to input ports, and S_{22} relates output ports to output ports. Figure 1.1 illustrates the described concepts.

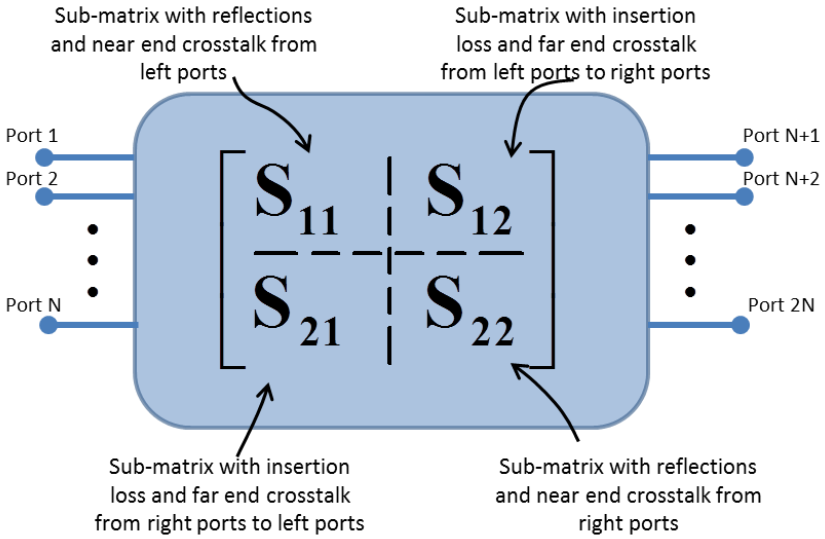

Figure 1.1. S-parameters of an Electrical Linear Network

1.1.3. Sources of Error in Channel Characterization Data. The main sources of the channel characterization data are measurements, full-wave simulations and analytical models. However, none of them provide ideal data. Measurements always have noise from various sources; the results are band limited and can only be obtained at a finite discrete set of points. Analytical models use mathematical approximations, simplify the reality and do not include all possible components of a system. Futher, there are very few geometries that can be accurately expressed by an analytical model. Full-wave simulations also use mathematical assumptions, but also are limited in their accuracy by numerical errors and the inherent discrete nature of a computer based simulation.

Any data that is available for describing a physical system is not perfectly accurate and does not describe it comprehensively. It is important to be able to estimate the quality of existing data in order to assess the reliability of the results and conclusion developed based on it. Simulation procedures used to assess signal integrity of a given

system are highly sensitive to the data they use. If the data violates important physics properties of real systems, the results can be nonsense and wrong decisions can be made affecting product design. This work is dedicated to three important properties of physical systems: passivity, reciprocity and causality - and studies the algorithms for checking and enforcing these properties on the data. In addition, issues of overall data handling for accurate system modeling, such as the extrapolation and interpolation of frequency domain data, are discussed.

1.2. PASSIVITY AND RECIPROCITY OF LINEAR NETWORKS

1.2.1. Definitions of Passivity and Reciprocity. High-speed interconnected systems do not contain active devices and, thus, are passive because they do not generate energy. In other words, the total energy of the output has to be less than or equal to the energy of the input at any point of time. The energy of a time domain signal $r(t)$ at the time point τ is defined as [1]:

$$E_r(\tau) = \int_{-\infty}^{\tau} [r(t)]^2 dt. \tag{9}$$

Then, if $u(t)$ is an input of the system and $v(t)$ is its output, then the following inequality has to hold:

$$E_u(\tau) - E_v(\tau) \geq 0, \forall \tau. \tag{10}$$

However, this time domain definition is not very practical, because it requires data for the entire time domain from $-\infty$ to $+\infty$ that are not available in a measurement or simulation. Further, most of the network characterization data is presented in frequency domain and therefore an equivalent definition for the frequency domain is necessary. The following necessary condition on the S-parameter matrix is defined in [4] and [5] that can be used to check for and enforce passivity. If $S(\omega)$ is a scattering matrix of a passive system, then

$$|\lambda_k| \leq 1, \forall k, \tag{11}$$

where λ_k is an eigenvalue of $[S^* \cdot S]$.

As also shown in [4], passive systems are reciprocal which means the response at port i on the excitation at port j is the same as the response at port j on the equivalent excitation at port i. In terms of S-parameters the following condition defines reciprocity:

$$S_{ij}(\omega) = S_{ji}(\omega), \forall i, j, \omega. \tag{12}$$

1.2.2. Metrics for Passivity and Reciprocity Quantification. In order to quantify the quality of the model in terms of passivity and causality, a formal metric has to be used. The following formulas presented in [5] can be used to define the passivity quality measure (PQM)

$$PQM = \max\left[\frac{N - \sum_{n=1}^{N} PW_n}{N}\right] \times 100\%, \tag{13}$$

where

$$PW_n = \max\left(\frac{\sqrt{\max\left[Eigenval\left(S^*(\omega_n) \cdot S(\omega_n)\right)\right]} - 1.0001}{0.1}, 0\right). \tag{14}$$

Similarly, the reciprocity quality measure (RQM) is defined in [5] as:

$$RQM = \max\left[\frac{N - \sum_{n=1}^{N} RW_n}{N}\right] \times 100\%, \tag{15}$$

where

$$RW_n = \max\left(\frac{\frac{1}{N_s}\sum_{i,j}\left|S_{ij}(\omega_n) - S_{ji}(\omega_n)\right| - 10^{-6}}{0.1}, 0\right). \quad (16)$$

1.2.3. Methods for Enforcing Passivity and Reciprocity. If the reciprocity violation is too large, data should not be used at all. Measurements will have to be repeated or the simulation redone more carefully. However, in case of a tolerable reciprocity violation, a system's reciprocity can be enforced simply by either copying the half above the main diagonal of the S-parameter matrix to the corresponding lower part or, alternatively, averaging reciprocal components and assigning the mean value to both of them. Either method works well and does not have significant benefits over the other.

On the contrary, passivity enforcement is a complicated operation. There are two main approaches to the passivity enforcement. The first approach is related to the vector fitting algorithm, discussed in details in the section 3.2.1. Following this approach, tabulated transfer function is approximated by the rational function with poles and residues. As shown in [6], poles and residues can be chosen in such a way that the result fitted transfer function is passive. The second approach is to modify the S-parameters matrix in every frequency sample by a series of iterative perturbations to enforce conditions (11) by using singular value decomposition and assigning the highest eigenvalue either to one [7] or to an optimized value less or equal than one [8]. These methods are iterative and have a learning rate parameter. Determining a good value for this parameter is a difficult task, since a very large value will prevent convergence, while the small value will make the procedure too long and inefficient.

1.3. CAUSALITY OF LINEAR NETWORKS

1.3.1. Causality Definition. Causality is a property of a physical system that reflects an intuitive notion of cause and consequence. Specifically, no system output can be observed before the input was applied. As was discussed above, a linear network can be defined in time domain by its impulse response $h(t)$. Then causality can be expressed as the following condition on impulse response:

$$h(t) = 0, \forall t \leq \tau. \tag{17}$$

While all physical systems are causal, the data that was obtained by measurements or simulations does not necessarily satisfy the condition above. Common reasons for causality violations are band limitations, finite sampling rate, measurement errors, and simulation approximations. There are three given impulse responses in Figure 1.2. The red curve corresponds to causal impulse response, but the green and blue ones are non-causal.

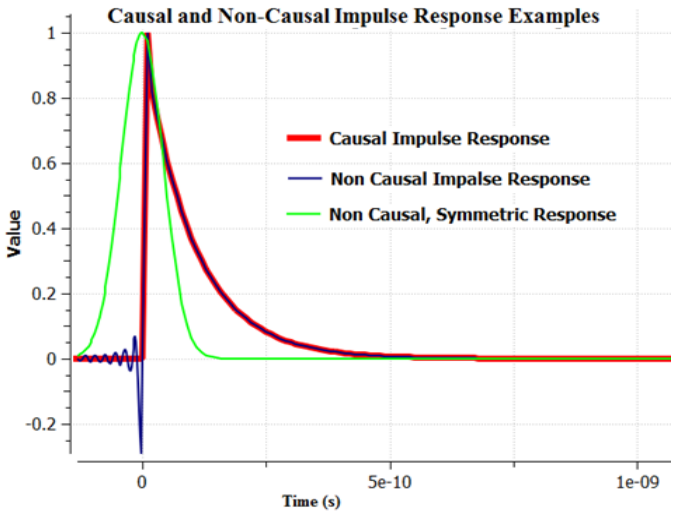

Figure 1.2. Examples of Causal and Non-Causal Impulse Responses

Usually, oscillated the causality violation near $t \leq 0$ moment is caused by frequency band limitation or measurement error at high frequencies for the corresponding transfer function (see the blue curve in Figure 1.2), but a causality violation similar to the green curve can be caused by a wrong simulation model.

1.3.2. Delay Causality. Physical systems have time delay. It takes a finite amount of time for input to propagate through the system before the output may be observed. Therefore, a physically valid system model should be not only causal, but delay causal. In terms of impulse response, delay causality property can be expressed using the following formula:

$$h(t) = 0, \forall t \leq \tau, \tag{18}$$

where τ is a time delay of the system. Delay causality is a more general concept than causality. Causality is just a special case with $\tau = 0$. For this reason, all the following results and discussions will be about delay causality, but they also apply to causality.

1.3.3. Metric for Delay Causality Quantification. Non-causality of the data is evidence of a discrepancy between the model and the modeled system. When the discrepancy is large, model assembly and simulation becomes difficult, may even fail, and the results become invalid and untrustworthy. However, a small discrepancy can still leave results in the acceptable error band. It is important to have a quantitative causality metric. Delay causality is related to the portion of the energy of the signal which comes at the output of the system before the delay time. Because of this, it is natural to define non-causality of the system as a square root of a ratio of the energy which comes before the delay to the total energy:

$$Non\text{-}causality\ \{h\} = \sqrt{\frac{\int_{-\infty}^{\tau} h^2(t)dt}{\int_{-\infty}^{\infty} h^2(t)dt}} \times 100\%. \tag{19}$$

A pictorial explanation of non-causality of the impulse response is given in Figure 1.3.

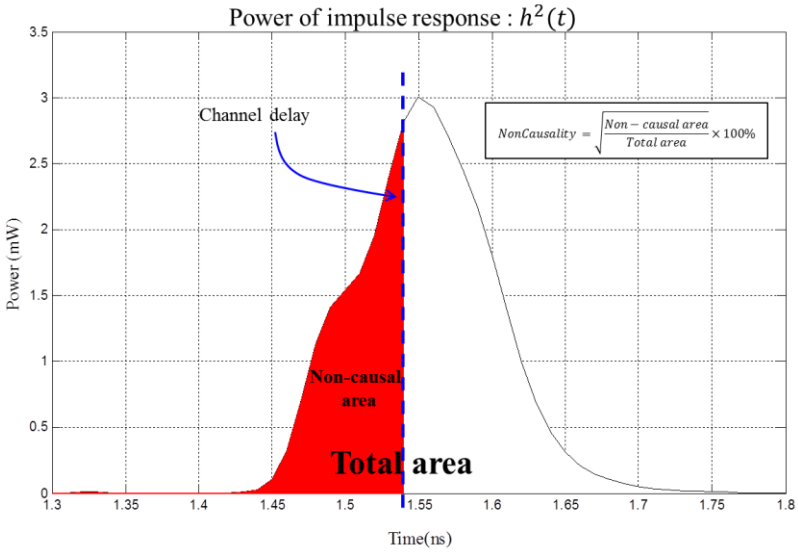

Figure 1.3. Pictorial Explanation of the Non-Causality Metric

Impulse response includes all frequency components. If the physical system is designed for a specific type of signal (with specific rise/fall time and bit rate), then it might be more useful instead of definition (19) of the non-causality metric to use the following definition:

$$Non\text{-}causality\{h\} = \sqrt{\frac{\int_{-\infty}^{\tau} r^2(t)dt}{\int_{-\infty}^{\infty} r^2(t)dt}} \times 100\%. \tag{20}$$

Here, $r(t)$ is a pulse response of the system:

$$r(t) = \int_{-\infty}^{\infty} h(t-s)v(s)ds \tag{21}$$

where $v(s)$ is an input pulse signal with specific rise/fall time and bit rate. The metric defined by (19) is called causality estimation and the metric defined by (20) is called pulse causality estimation. It is important to note that in practice the approximation of

these metrics are used. The data is almost always available only over the limited time interval and at the discrete points. Therefore, the integrals above are numerically approximated and signals and impulse responses are assumed to be zero outside the given time interval. These limitations have to be carefully handled for the approximation to be accurate.

An example of the proposed metric is shown below. Both causality and pulse causality estimation were calculated for the measured differential insertion loss of a 1.2 in microstrip with 2.4 mm SMA connectors and 6 in cables at each side. The detailed geometry model of the microstrip is shown in Figure 1.4.

Figure 1.4. Geometry of the DUT Structure

The magnitude of differential insertion loss for the DUT is shown below in Figure 1.5. Calculated causality estimation for the differential insertion loss of the given geometry is equal to 89%, but pulse causality estimation is equal to 99.9% (pulse signal was taken with 16 ps rise/fall time and 12.5 Gbps bit rate). Figure 1.6 shows causality and pulse causality violations for differential insertion loss of the measured S-parameters of the structure given in Figure 1.4.

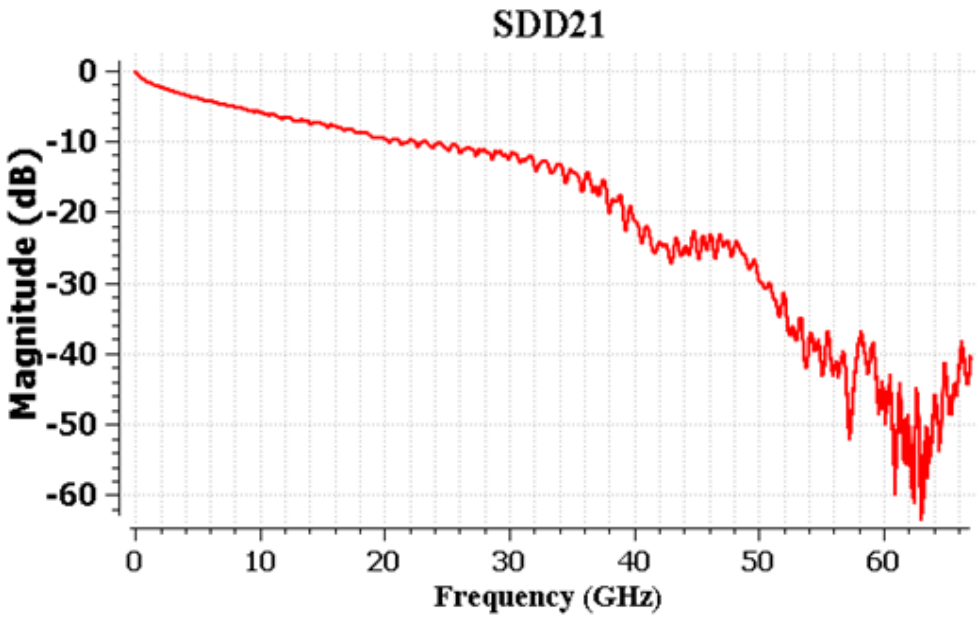

Figure 1.5. Differential Insertion Loss for the Geometry Given in Figure 1.4

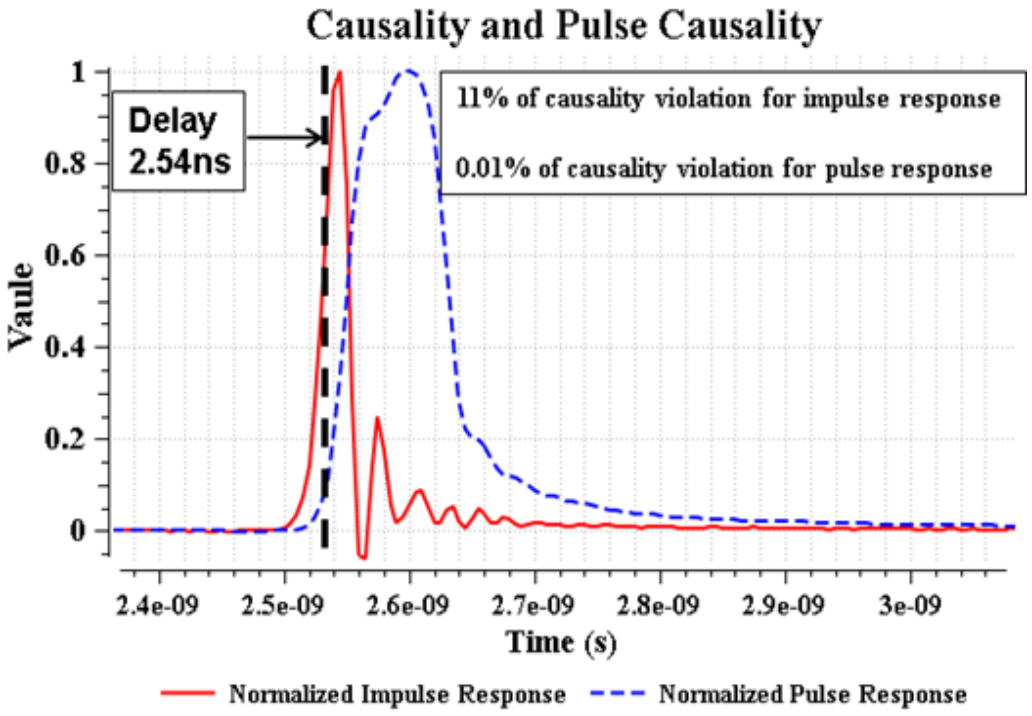

Figure 1.6. Causality and Pulse Causality Violations for Differential Insertion Loss for the Structure Given in Figure 1.4

Therefore, an 11% causality violation for the insertion loss is related to high frequency components (more than 12.5 Gbps speed signals contained) and if the system is manufactured for less than 12.5 Gbps speed signals, then the model can be considered almost 100% causal.

2. FREQUENCY DOMAIN METHODS FOR CHECKING AND ENFORCING CAUSALITY

2.1. KRAMERS-KRONIG RELATIONS FOR CAUSAL SYSTEMS

2.1.1. Definition and Derivation of Kramers-Kronig Relations. Definition of causality is naturally formulated in terms of time domain system characterization – impulse response. However, in modern electrical systems modeling the data is often given in frequency domain. It has a lot of advantages for thorough accurate and efficient modelling, simulation and analysis. Therefore, it becomes important to find a condition a frequency domain system characterization that is equivalent to system causality. The following derivations result in such condition in terms of system's transfer function. Impulse response $h(t)$ will satisfy causality condition if and only if it satisfies the following relation:

$$h(t) = h(t)sign(t),\ t \in (-\infty, \infty). \tag{22}$$

Let $H(\omega)$ be a transfer function corresponded to the impulse response $h(t)$*:*

$$H(\omega) = \mathbb{F}\{h(t)\} = \int_{-\infty}^{\infty} h(t)e^{-j\omega t}dt, \tag{23}$$

where $\mathbb{F}\{h(t)\}$ is the Fourier transform operator. Combining (22) and (23) and using the convolution theorem (see [2], p. 27, (2-74)), it follows that the transfer function $H(\omega)$ will satisfy the following equation:

$$H(\omega) = \mathbb{F}\{h(t)sign(t)\} = \frac{1}{2\pi}\mathbb{F}\{h(t)\} * \mathbb{F}\{sign(t)\} = \frac{1}{2\pi}H(\omega) * \frac{2}{j\omega}$$

$$H(\omega) = \frac{1}{j\pi}\int_{-\infty}^{\infty}\frac{H(\omega\prime)}{\omega-\omega\prime}d\omega', \tag{24}$$

where "$*$" denotes the convolution operator. The transformation of a function that appears at the end of the derivation is called a Hilbert transform. Further, the following notation is used:

$$\mathbb{H}\{u\}(\omega') \stackrel{\text{def}}{=} \frac{1}{\pi}\int_{-\infty}^{\infty}\frac{u(\omega)}{\omega'-\omega}d\omega \tag{25}$$

Summarizing the derivations above, the causality of a system can be expressed as a following condition of its transfer function:

$$H(\omega) = -j\mathbb{H}\{H\}(\omega). \tag{26}$$

Transfer function $H(\omega)$ is a complex function. Hence it can be represented as $H(\omega) = Re(\omega) + jIm(\omega)$, where Re and Im are its real and imaginary parts, respectively. Then, (26) can be rewritten as follows using the linearity of the Hilbert transform:

$$\begin{aligned} Re(\omega) + jIm(\omega) &= -j\mathbb{H}\{Re + jIm\}(\omega) \\ &= -j\mathbb{H}\{Re\}(\omega) + \mathbb{H}\{Im\}(\omega). \end{aligned} \tag{27}$$

Equating real and imaginary parts of (27), the following relations are obtained:

$$\begin{aligned} Re(\omega) &= \mathbb{H}\{Im\}(\omega) \\ Im(\omega) &= -\mathbb{H}\{Re\}(\omega). \end{aligned} \tag{28}$$

These relations are called Kramers-Kronig relations between the real and imaginary parts of the transfer function of a causal system. The relations show that the real part can be uniquely determined from the imaginary part and the imaginary part can be uniquely determined from the real part, which provides the foundation for causality checking and the enforcing algorithm discussed in the next chapter.

Alternatively, the transfer function can be represented as $H(\omega) = \rho(\omega)e^{-j\varphi(\omega)} = e^{-(\alpha(\omega)+j\varphi(\omega))}$, where $\alpha(\omega)$ is a logarithm of the transfer function's magnitude and $\varphi(\omega)$ is its phase. Assuming there are no frequency points for which $H(\omega) = 0$, relation (26) is also true for the logarithm of transfer function: $ln\big(H(\omega)\big) = -\big(\alpha(\omega) + j\varphi(\omega)\big)$. That produces the Kramers-Kronig relations between the magnitude and phase of a transfer function of a causal system [2]:

$$\alpha(\omega') = \alpha(0) - \frac{\omega_0^2}{\pi}\int_{-\infty}^{\infty}\frac{\varphi(\omega)}{\omega(\omega^2 - (\omega')^2)}d\omega \tag{29}$$

$$\varphi(\omega') = \frac{\omega'}{\pi}\int_{-\infty}^{\infty}\frac{\alpha(\omega)}{\omega^2-(\omega')^2}d\omega = -\frac{1}{\pi}\int_{-\infty}^{\infty}\frac{\alpha(\omega)}{\omega'-\omega}d\omega. \tag{30}$$

Here, $\varphi(\omega)$ is a phase transfer function. It is important to note that the phase can be uniquely determined from the magnitude only for the minimal phase systems. Formally, the minimal phase system is defined as a system in which the transfer function has both poles and zeros inside the unit circle [1]. However, a more insightful description can be made through one of the properties of a minimal phase function. It can be shown that any transfer function can be decomposed into the product of a minimal phase system transfer function with the same magnitude and the transfer function with unity magnitude and nonzero phase:

$$H(\omega) = H_{min}(\omega)H_1(\omega). \tag{31}$$

It can be shown that $\arg H_1(\omega)$ is negative [9] and thus:

$$\arg H(\omega) < \arg H_{min}(\omega). \tag{32}$$

The phase delay of a system is defined as:

$$\tau_p(\omega) = -\frac{\varphi(\omega)}{\omega}, \tag{33}$$

where $\varphi(\omega)$ is a phase of a system's transfer function. The group delay of a system is defined as:

$$\tau_g = \lim_{\omega \to \infty} \tau_p(\omega)\,. \tag{34}$$

By combining (32) and (34), it is seen that $H_{min}(\omega)$ is a function which has the smallest group out of possible functions with the magnitude equal to the magnitude of $H(\omega)$. Therefore, the second term $H_1(\omega)$ basically represents a time shift.

For a minimal phase system, (30) shows that phase now can be uniquely determined from the magnitude. Further, a system can be reduced to a minimal phase system by extracting the delay which provides an opportunity for another method for causality checking and enforcing.

2.1.2. Numerical Calculation of the Hilbert Transform. Let $U(\omega)$ and $V(\omega)$ satisfy the following relation:

$$V(\omega') = \frac{1}{\pi}\int_{-\infty}^{\infty} \frac{U(\omega)}{\omega' - \omega}\, d\omega. \tag{35}$$

For the given frequency points $\{\omega_0, \omega_1, \dots, \omega_N\}$ and corresponding values $\{U_0, U_1, \dots, U_N\}$, the values of $\{V_0, V_1, \dots, V_N\}$ have to be calculated. The transfer function of a linear network satisfies the following equation:

$$H(-\omega) = H^*(\omega). \tag{36}$$

Whether U is the real part or the magnitude, it is an even function and $U(-\omega) = U(\omega)$. Therefore, the known frequency band can be extended into the corresponding negative frequencies. Integral (35) is taken over the infinite frequency interval, but

because of the frequency band limitation it can only be calculated up to the maximum given frequency ω_N:

$$V(\omega') = \frac{1}{\pi}\int_{-\omega_N}^{\omega_N} \frac{U(\omega)}{\omega' - \omega} d\omega + Err(\omega'). \tag{37}$$

The error will be equal to the integral outside the frequency band:

$$Err(\omega') = \frac{1}{\pi}\int_{-\infty}^{-\omega_N} \frac{U(\omega)}{\omega' - \omega} d\omega + \frac{1}{\pi}\int_{\omega_N}^{\infty} \frac{U(\omega)}{\omega' - \omega} d\omega. \tag{38}$$

Assuming that the system is passive, the norm of the real part (as well as of the magnitude) of the transfer function is less than one for all the frequency samples. The error can then be estimated by the following inequality

$$|Err(\omega')| \leq \left|\log \frac{\omega_N - \omega'}{\omega_N + \omega'}\right|. \tag{39}$$

The error is equal to zero for $\omega' = 0$, is small near DC, and tends to infinity when ω' is approaching ω_N which means the calculations near maximum frequency will be inaccurate. In order to solve this numerical instability, the Kramers-Kronig relations with subtractions can be used.

2.1.3. Kramers-Kronig Relations with Subtractions. The relations obtained previously can be generalized for a set of so-called subtraction points. If two functions $U(\omega)$ and $V(\omega)$ satisfy the Kramers-Kronig relations, then, as it was shown in [10] and [11], for a set of frequency points $\{\sigma_0, \sigma_1, \ldots, \sigma_M\}$ called subtraction points, the following relations hold:

$$V(\omega') - L_V(\omega') = -\frac{\prod_{q=1}^{M}(\omega' - \sigma_q)}{\pi}\int_{-\infty}^{\infty} \frac{U(\omega) - L_U(\omega)}{\prod_{q=1}^{M}(\omega - \sigma_q)} \frac{d\omega}{\omega' - \omega} \tag{40}$$

where $L_V(\omega)$ and $L_U(\omega)$ are Lagrange polynomials of functions $V(\omega)$ and $U(\omega)$, respectively, constructed in the set of subtraction points. Using this generalized formulation, function $V(\omega)$ can be reconstructed from $U(\omega)$:

$$V(\omega') = L_V(\omega') - \frac{\prod_{q=1}^{M}(\omega' - \sigma_q)}{\pi} \int_{-\infty}^{\infty} \frac{U(\omega) - L_U(\omega)}{\prod_{q=1}^{M}(\omega - \sigma_q)} \frac{d\omega}{\omega' - \omega}. \quad (41)$$

This method was proposed in [11] for checking causality using the real part of a transfer function $U(\omega)$ to reconstruct the imaginary part $V(\omega)$ and the difference between the given imaginary and reconstructed parts was used to quantify causality. However, in the proposed method, a Lagrange polynomial $L_V(\omega)$ is constructed based on the values of the original imaginary part which is acceptable for causality checking, but makes direct application of this method for causality enforcement impossible. Nevertheless, the generalization of that approach opens an entire class of methods for enforcing causality. Further sections describe the general approach and some of the specific methods from the class.

2.2. MORE CAUSALITY CONDITIONS FOR A TRANSFER FUNCTION OF LINEAR ELECTRICAL NETWORK

2.2.1. Paley-Wiener Theorem and Its Implications. In addition to Kramers-Kronig relations, causality of impulse response $h(t)$ implies more conditions for the corresponding transfer function $H(\omega) = Re(\omega) + jIm(\omega) = \rho(\omega)e^{-j\varphi(\omega)}$. The impulse response of a linear electrical network is assumed to have finite energy based on the physics of a modeled system. This implies that the magnitude of the transfer function is square-integrable:

$$\int_{-\infty}^{\infty} \rho^2(\omega) d\omega < \infty. \quad (42)$$

The following theorem formulates a necessary and sufficient condition for a square-integrable function to be a magnitude of a transfer function of a causal system.

Paley-Wiener Theorem. [2] For a real valued square-integrable function $\rho(\omega)$, there exists a corresponding function $\varphi(\omega)$ such that the function $H(\omega) = \rho(\omega)e^{-j\varphi(\omega)}$ is a Fourier image of a causal impulse response $h(t)$ if, and only if, the following integral is finite:

$$\int_{-\infty}^{\infty} \frac{|ln\,\rho(\omega)|}{1+\omega^2} < \infty. \tag{43}$$

It is important to note, that this condition does not provide a complete method for checking causality. If the magnitude of $H(\omega)$ satisfies (43), it does not mean that $H(\omega)$ is a transfer function of a causal system. It only means that there exists corresponding phase function such that the resulting function will describe a causal system. There are several important implications from the Paley-Wiener theorem.

Corollary 1. If $h(t)$ is a causal impulse response with nonzero energy, then the corresponding transfer function $H(\omega)$ cannot be zero in any interval:

$$\nexists(\omega_1, \omega_2): H(\omega) = 0\ \forall\omega \in (\omega_1, \omega_2). \tag{44}$$

Proof. If $H(\omega) = 0$ in (ω_1, ω_2), then $\rho(\omega) = 0$ in (ω_1, ω_2). $ln(0) = \infty$ and consequentially:

$$\int_{-\infty}^{\infty} \frac{|ln\,\rho(\omega)|}{1+\omega^2} \geq \int_{\omega_1}^{\omega_2} \frac{|ln\,\rho(\omega)|}{1+\omega^2} = \int_{\omega_1}^{\omega_2} \frac{|ln\,0|}{1+\omega^2} = \infty. \tag{45}$$

Corollary 2. If $H_1(\omega)$ and $H_2(\omega)$ are transfer functions of a causal system with corresponding impulse responses $h_1(t)$ and $h_2(t)$ and there exists an interval (ω_1, ω_2) in which they are the equal, then these functions are equal on the entire frequency range.

Proof. If $h_1(t)$ and $h_2(t)$ are causal, then $h_1(t) - h_2(t)$ is also causal. The Fourier transform is linear and so $\mathbb{F}\{h_1(t) - h_2(t)\} = H_1(\omega) - H_2(\omega)$. As a transfer

function of a causal system the only way $H_1(\omega) - H_2(\omega)$ can have zero magnitude in an interval is if it is an identical zero on the entire frequency range.

Corollary 3. The following asymptotical equation has to hold:

$$\exists(0 < \varepsilon < 1): |\rho(\omega)| = o(\omega^{1-\varepsilon}),\ \omega \to \infty. \tag{46}$$

2.2.2. Causality and Linear Phase Systems. A perfectly linear phase is a common approximation for the simplicity of modeling and prototyping. However, it turns out that such approximation violates causality and thus can invalidate simulation results. The thorough analysis of this phenomenon is presented in this section.

Delay causal systems can't have perfectly linear phase, if magnitude is frequency dependent. Let $H(\omega) = \rho(\omega)e^{-j\omega\tau}$ be a transfer function with a linear phase and frequency dependent magnitude, where τ is a delay of the system. Impulse response $h(t)$ of transfer function $H(\omega)$ is calculated using the inverse Fourier transform:

$$h(t) = \frac{1}{2\pi}\int_{-\infty}^{\infty} H(\omega)e^{j\omega t}d\omega. \tag{47}$$

Further,

$$\begin{aligned} h(t) &= \frac{1}{2\pi}\int_{-\infty}^{0} H(\omega)e^{j\omega t}dt + \frac{1}{2\pi}\int_{0}^{\infty} H(\omega)e^{j\omega t}dt \\ &= \frac{1}{2\pi}\int_{0}^{\infty}\left(H(-\omega)e^{-j\omega t} + H(\omega)e^{j\omega t}\right)d\omega. \end{aligned} \tag{48}$$

Using the fact that $H(-\omega) = H^*(\omega)$, it can be derived that:

$$h(t) = \frac{1}{2\pi}\int_{0}^{\infty} \rho(\omega)\left(e^{j\omega(\tau-t)} + e^{-j\omega(\tau-t)}\right)d\omega. \tag{49}$$

From (49), $h(t+\tau)$ can be calculated:

$$h(\tau + t) = \frac{1}{2\pi}\int_0^\infty \rho(\omega)\left(e^{j\omega t} + e^{-j\omega t}\right)d\omega. \quad (50)$$

Analogously,

$$h(\tau - t) = \frac{1}{2\pi}\int_0^\infty \rho(\omega)\left(e^{j\omega t} + e^{-j\omega t}\right)d\omega. \quad (51)$$

Therefore, $h(\tau + t) = h(\tau - t)$, which means the impulse response is symmetric regarding τ and if there is some response after τ, there should be the same response before it. If the impulse response is delay causal then $h(\tau - t)$ is equal to zero for all positive t. In this case, $h(\tau + t)$ should be also equal to zero. It is possible if, and only if, the impulse response is a delta function (centered at τ) which results in the magnitude of the transfer function being frequency independent.

It is shown below that a small perturbation of the phase for network parameters can significantly change the impulse response. Three different insertion losses are constructed: the first, S_{DD_1}, is the original differential insertion loss for the geometry given in Figure 1.4; the second, S_{DD_2}, is the insertion loss with the same magnitude as the original one, but the phase is perfectly linear; the third, S_{DD_3}, is the insertion loss with the same amplitude as the original one, but the phase is equal to a perfectly linear phase plus the reversed nonlinear part of the original one. Figure 2.1 and Figure 2.2 show that all three cases have absolutely the same amplitudes and the maximal difference between phases is equal to 0.2%. Impulse responses for all three cases are shown in Figure 2.3. The blue curve corresponds to the original insertion loss S_{DD_1}; the red curve corresponds to the insertion loss with a perfectly linear phase S_{DD_2} (nonlinear part of the phase is removed from S_{DD_1}); and the green curve corresponds to S_{DD_3} insertion loss (nonlinear part of the phase in S_{DD_1} that is reversed).

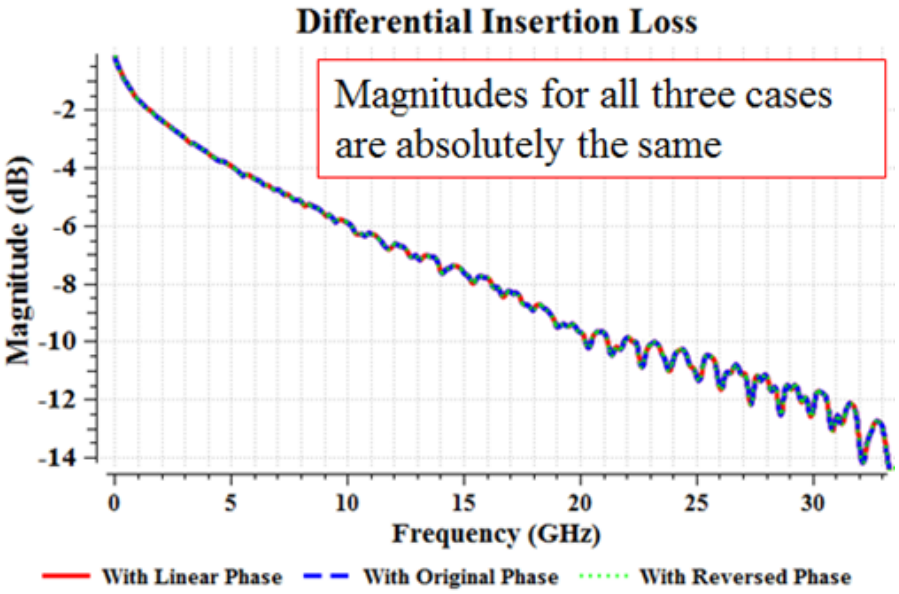

Figure 2.1. Magnitudes for S_{DD_1}, S_{DD_2}, and S_{DD_3} Insertion Losses

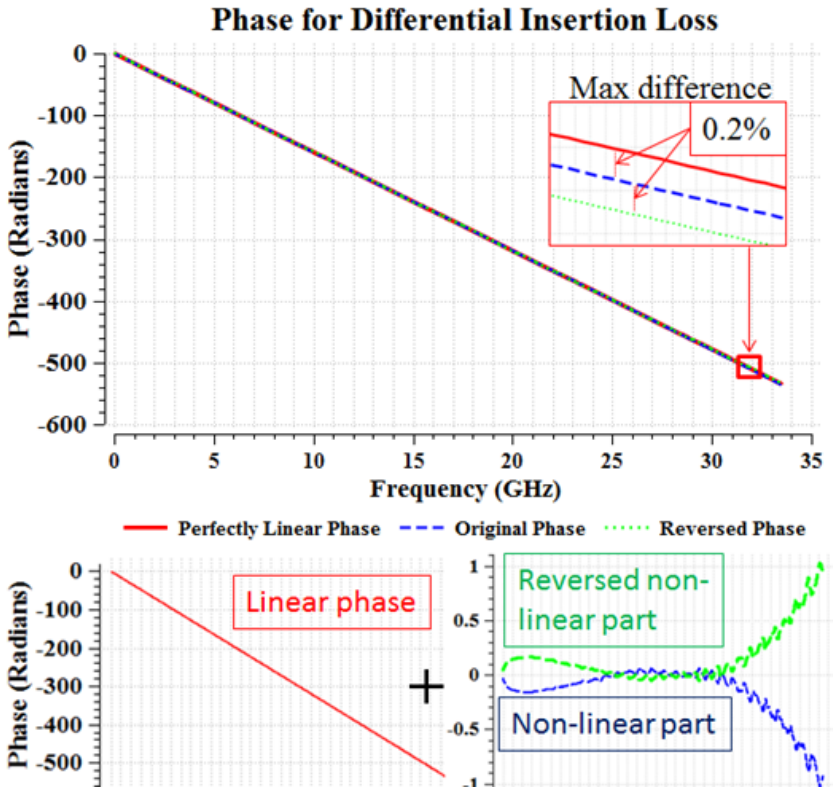

Figure 2.2. Unwrapped Phases for S_{DD_1}, S_{DD_2}, and S_{DD_3} Insertion Losses

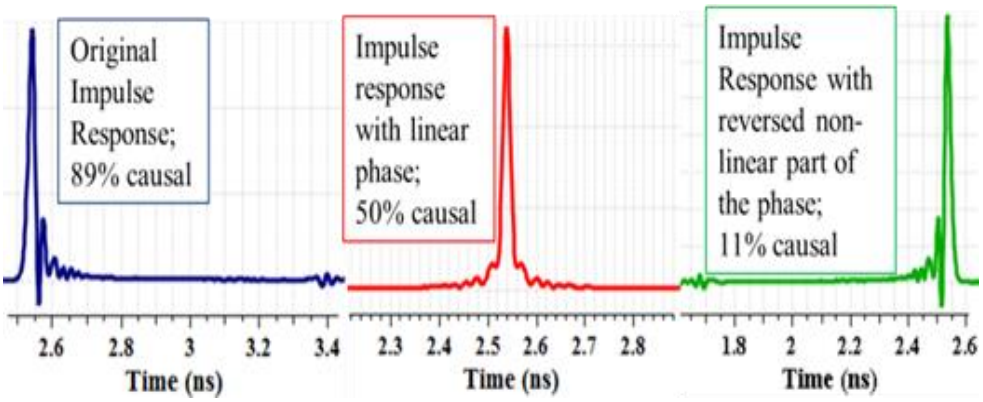

Figure 2.3. Impulse Responses Corresponding to S_{DD_1} (original insertion loss), S_{DD_2} (insertion loss with linear phase), and S_{DD_3} (insertion loss with reversed nonlinear part of the phase)

Even though magnitudes for all three cases are absolutely the same and the difference between phases is small, the shapes of the corresponding impulse responses are absolutely different. The original impulse response is physical as the causality is equal to 89% and the impulse responses with a linear phase and reversed nonlinear part of the phase are nonphysical. Causality of the impulse response with a linear phase is equal to 50% and causality of the impulse response with reversed nonlinear part of the phase is equal to 11%. One of the implications of this is that if there is a causality violation for network parameters, it is possible to make a small perturbation in the phase that improves causality of the system function without changing the magnitude.

2.3. DELAY CAUSALITY ENFORCEMENT USING KRAMERS-KRONIG RELATIONS

Kramers-Kronig relations (28), (29), and (30) derived previously suggest a methodology for checking and enforcing causality of a linear network model: take a transfer function, separate it into two corresponding parts, and reconstruct one of the parts using the other by enforcing Kramers-Kronig relations. There are four possible approaches: reconstruct the phase from the magnitude, the imaginary part from the real part, or the real part from the imaginary part, and if the DC value of the magnitude is known then the rest can be reconstructed from the phase. However, as it is shown further,

only the first two approaches are practical for sampled, band-limited data. The following formulas define reconstruction:

$$\varphi(\omega') = \frac{\omega'}{\pi}\int_{-\infty}^{\infty}\frac{\alpha(\omega)}{\omega^2-(\omega')^2}d\omega = \frac{1}{2\pi}\int_{-\infty}^{\infty}\frac{\alpha(\omega)}{\omega-\omega'}d\omega - \frac{1}{2\pi}\int_{-\infty}^{\infty}\frac{\alpha(\omega)}{\omega+\omega'}d\omega \quad (52)$$

$$Im(\omega') = \frac{1}{\pi}\int_{-\infty}^{\infty}\frac{Re(\omega)}{\omega\prime-\omega}d\omega. \quad (53)$$

Both approaches require numerical calculation of the Hilbert transform. The following section describes the initial approach for such a calculation and its challenges.

2.3.1. General Method for Enforcing Kramers-Kronig Relations with Subtractions. This section describes a general approach for reconstructing a function from its Kramers-Kronig relations counterpart using the subtractions technique.

For given frequency points $\{\omega_0, \omega_1, \dots, \omega_N\}$ and corresponding values $\{U_0, U_1, \dots, U_N\}$, the values of $\{V_0, V_1, \dots, V_N\}$ have to be calculated. At each frequency point of interest ω_k, a set of corresponding subtraction frequency points $\{\sigma_0^k, \sigma_1^k, \dots, \sigma_{M_k}^k\}$ are defined. L_V^k and L_U^k are Lagrange polynomials of functions V and U, respectively, constructed in the corresponding set of subtraction points. These points are selected from the given frequency data set so that the values of functions V and U are known in them and the Lagrange polynomials can be constructed. Then Kramers-Kronig relations with subtractions (41) can be written as follows:

$$V(\omega_k) = L_V^k(\omega_k) - \frac{\prod_{q=1}^{M_k}(\omega_k-\sigma_q^k)}{\pi}\left[\int_{-\omega_N}^{\omega_N}\frac{U(\omega)-L_U^k(\omega)}{\prod_{q=1}^{M_k}(\omega-\sigma_q^k)}\frac{d\omega}{\omega_k-\omega} + \int_{\Omega_N}\frac{U(\omega)-L_U^k(\omega)}{\prod_{q=1}^{M_k}(\omega-\sigma_q^k)}\frac{d\omega}{\omega_k-\omega}\right], \quad (54)$$

where $\Omega_N = (-\infty, -\omega_N) \cup (\omega_N, \infty)$. The following derivation provides more details of the term $V(\omega_k) - L_V^k(\omega_k)$:

$$V(\omega_k) - L_V^k(\omega_k) = V_k - \sum_{q=1}^{M_k} V\left(\sigma_q^k\right) \prod_{\substack{p=1 \\ p \neq q}}^{M_k} \frac{\omega_k - \sigma_p^k}{\sigma_q^k - \sigma_p^k}. \quad (55)$$

Since subtraction points belong to the given frequency points set, $V\left(\sigma_q^k\right) = V_m$ for some m. Then, (55) can be rewritten as an inner product of the vector $\bar{V}$ of unknown values V_k and the vector $\overline{M_k}$, where the m^{th} element of this vector is:

$$\overline{M_k}_m = \begin{cases} -\prod_{\substack{p=1 \\ p \neq q}}^{M_k} \frac{\omega_k - \sigma_p^k}{\omega_m - \sigma_p^k}, \omega_m \; is \; a \; subtraction \; for \; \omega_k, m \neq k \\ 1, \; m = k \\ 0, otherwise \end{cases}. \quad (56)$$

Finally, expression (54) can be rewritten in the following matrix form:

$$\bar{\bar{M}} \cdot \bar{V} = -\frac{1}{\pi}(\bar{I} + \bar{L} + \bar{E}). \quad (57)$$

The following notation is used in the formula above:

- $\bar{V}$ is a vector of unknown values V_k;
- $\bar{\bar{M}}$ is a matrix where each row is a corresponding vector $\overline{M_k}$;
- $\bar{I}$ is a vector of the right side integral within the given frequency range. It can be calculated semi-analytically using a linear approximation of $U(\omega)$:

$$I_k = \int_{-\omega_N}^{\omega_N} \frac{\prod_{q=1}^{M_k}(\omega_k - \sigma_q^k)}{\prod_{q=1}^{M_k}(\omega - \sigma_q^k)} \frac{U(\omega) - L_U^k(\omega)}{\omega_k - \omega} d\omega. \quad (58)$$

- $\bar{L}$ is a vector of integrals of $L_U^k(\omega)$ over the outside the frequency range. It is an integral of a rational function and can be calculated analytically.

$$L_k = -\int_{\Omega_{\omega_N}} \frac{\prod_{q=1}^{M_k}(\omega_k - \sigma_q^k)}{\prod_{q=1}^{M_k}(\omega - \sigma_q^k)} \frac{L_U^k(\omega)}{\omega_k - \omega} d\omega \tag{59}$$

• $\bar{E}$ is a vector of integrals of $U(\omega)$ outside the frequency range. In practice, $U(\omega)$ is not given outside the frequency range and has to be extrapolated. The extrapolated function is written as $\widetilde{U}(\omega)$ in the rest of this work.

$$E_k = \int_{\Omega_{\omega_N}} \frac{\prod_{q=1}^{M_k}(\omega_k - \sigma_q^k)}{\prod_{q=1}^{M_k}(\omega - \sigma_q^k)} \frac{\widetilde{U}(\omega)}{\omega_k - \omega} d\omega \tag{60}$$

After all the parts of the matrix equation (57) are calculated, it can be solved and new values of $V(\omega_k)$ are obtained. These values are an approximation to the Kramers-Kronig relations counterpart of $U(\omega)$ in the given frequency points ω_k.

The proposed class of methods can be used to reconstruct imaginary part from the real part of a transfer function or the phase from the magnitude of the transfer function to enforce causality. There are several parameters of this method that can be varied for a better performance and/or accuracy. The following section discusses these parameters and gives some guidelines on the choice of them.

2.3.2. Parameters of the Proposed Class of Methods for Enforcing Kramers-Kronig Relations. There are two important parameters in the method described above: a scheme of choosing subtraction points and the way $U(\omega)$ is extrapolated outside the given frequency range. Both of these parameters heavily affect the accuracy of the calculations and the reliability of the obtained causality enforced data. This section provides a general guideline for choosing these parameters as well as a detailed analysis of some practical cases.

2.3.2.1. Subtractions scheme. Using subtraction points adds stability to the calculations. Subtractions reduce the error caused by the limitation of the frequency band (see [11]). At the frequency points near DC the error is too small and a small number of subtractions is enough, but near the maximum frequency where the error becomes large

more subtractions might be necessary. However, there are two sources of errors in (54). The first is caused by the limitation of the frequency band and can be reduced by increasing the number of subtractions. The other error is in Lagrange polynomial L_V and is caused by using approximate values already calculated for the imaginary part. This error becomes larger with an increasing number of subtractions. From here it follows that increasing the number of subtractions reduces one error, but amplifies the other error and vice versa. It is important to find the optimal number of subtractions for (54), but this problem still remains open.

Since the Lagrange polynomial is defined in the same set of subtraction points, it is beneficial for reducing the Lagrange approximation error to include advance knowledge about the $V(\omega)$ function into the structure of the subtraction scheme. Specifically, it is known that:

$$V(-\omega) = -V(\omega). \tag{61}$$

Therefore, using opposite frequency points together will not increase the propagating approximation error while increasing the number of subtractions used and thus will decrease the integral instability error. Further, (61) implies that $V(0) = 0$, which means that using $\sigma = 0$ as a subtraction point is also beneficial since that guarantees that reconstructed $V(\omega)$ will have a correct value at zero. Lastly, the following trick can be applied: the front delay of a channel can be estimated as a linear part of the phase. The line that connects the first and the last given frequency point can be used as a linear part of the phase. When this line is subtracted in the delay extraction phase, the last phase value becomes zero. Putting another subtraction point there improves the stability of calculations without damaging the accuracy.

2.3.2.2. Extrapolation of *U(ω)*. Another important part of specifying the Kramer-Kronig based causality enforcement algorithm is an extrapolation technique for $U(\omega)$ outside the given frequency range. It has to satisfy two conditions to be physical:

continuity and the Paley-Wiener theorem. The following equations formalize these conditions:

$$\widetilde{U}(\omega_N) = U(\omega_N), \tag{62}$$

$$\left|\widetilde{U}(\omega)\right| = o(\omega^{1-\epsilon}), \omega \to \infty, 0 < \varepsilon < 1. \tag{63}$$

If these conditions are satisfied, then the Paley-Wiener theorem guarantees that there exists one, and only one, function $V(\omega)$ that is a causal counterpart of $U(\omega)$. Further, if the extrapolation is chosen in a way that the integration of E_k can be done analytically or at least tightly bound, then this error can be effectively compensated for and the accuracy of the overall causality enforcement technique becomes very good.

It is easy to comply with the first condition, while the second is more complicated. For this reason, existing techniques of extrapolation often violate it and will potentially lead to inaccurate nonphysical results in the calculation. However, for simplicity reasons it may still be acceptable in practical applications. The two most widespread non-causal techniques for extrapolation are constant extrapolation and its special case, zero extrapolation (often called zero padding). While both obviously violate the Paley-Wiener theorem (and zero extrapolation violates continuity as well), the inaccuracy may be tolerable in most practical cases. Constant extrapolation gives a chance to calculate E_k analytically and compensate for it which improves the accuracy of the causality enforcement technique.

Finally, the method proposed below gives a potential solution for a causal analytical extrapolation.

2.3.2.2.1 <u>Causal analytical extrapolation technique proposal.</u> One of the implications of the Paley-Wiener theorem is that values at a finite number of points do not define the causality of a function. Specifically, if the function is known only at finite number of points, it can always be defined in the rest of the domain in a way that it becomes causal. The causal extrapolation problem can be formulated for a given set of frequency points $\omega_0, \omega_1, \dots, \omega_N$ and corresponding values $H_0, H_1, \dots, H_N$ to find an analytical function $\widetilde{H}(\omega)$ such that it is causal and for any given point ω_k: $\widetilde{H}(\omega_k) = H_k$.

This problem currently remains open and this work does not fully solve it, however, the following framework for a potential solution is being proposed.

Let U_k and V_k be Kramers-Kronig counterparts associated with the given value H_k. Then, they satisfy Kramer-Kronig relations with subtractions from (55):

$$V_k = L_V^k(\omega_k) - [I_k + L_k + E_k]. \tag{64}$$

As was discussed previously, the matrix as well as the vectors I_k and L_k can be calculated semi-analytically. Let the extrapolated values of $U(\omega)$ that are integrated in the term E_k be the following sum:

$$\widetilde{U}(\omega) = \sum_{r=0}^{N} \alpha_r \sqrt[r+2]{\omega}. \tag{65}$$

If the corresponding integrals can be calculated analytically or at least tightly bound, the problem can be optimized over values of α_r to minimize the error between the values of V_k obtained through causality enforcement and the given data samples.

Special case of this technique is to use only one term, square root. This can be calculated analytically and directly applied to the described causality enforcement algorithm. Appendix A contains derivations of the error compensation term for this case.

2.3.3. Using Fast Fourier Transform for Efficient Enforcement of Kramers-Kronig Relations. Another method that can be used for enforcing Kramers-Kronig relations efficiently is the Fast Fourier transform (FFT) and the inverse Fourier transform (IFFT). As shown in (24), the Hilbert integral is a convolution. Convolution in frequency domain is equivalent to the multiplication in time domain [2]. Using this, the following equivalence can be derived [12], [13]:

$$\begin{gathered} g(\omega') = \mathbb{H}\{f(\omega)\} = \frac{1}{\pi}\int_{-\infty}^{\infty} \frac{f(\omega)}{\omega' - \omega} d\omega \\ g(\omega') = \frac{1}{\pi}\left(f(\omega) * \frac{1}{\omega}\right) = \mathbb{F}\{\mathbb{F}^{-1}\{f(\omega)\} \cdot \left(j \cdot \text{sign}(t)\right)\}, \end{gathered} \tag{66}$$

where $\mathbb{F}$ is the Fourier transform operator and $\mathbb{F}^{-1}$ is the inverse Fourier transform operator and t is a variable in the inverse Fourier transform domain. Using a discrete approach to calculate the Fourier transform and its inverse provides a way to substitute the Hilbert integral with the discrete Hilbert transform (DHT) defined as:

$$d\mathbb{H}\{f(\omega)\} = FFT\{IFFT\{f(\omega)\} \cdot (j \cdot \text{sign}(t))\}. \tag{67}$$

Thus, the calculation of the Hilbert integral is equivalent to the calculation of two Fourier transforms and function multiplication. As was shown in [13], this observation can be used for causality enforcement. The imaginary part can be reconstructed from the real part and the minimum phase can be reconstructed from the magnitude using this Fourier transform-based approach.

To illustrate the DHT-based causality enforcing algorithm, the following example was considered. A single-ended high-speed link containing SMA connectors and a stripline was measured. Figure 2.4 shows the magnitude and phase of its insertion loss.

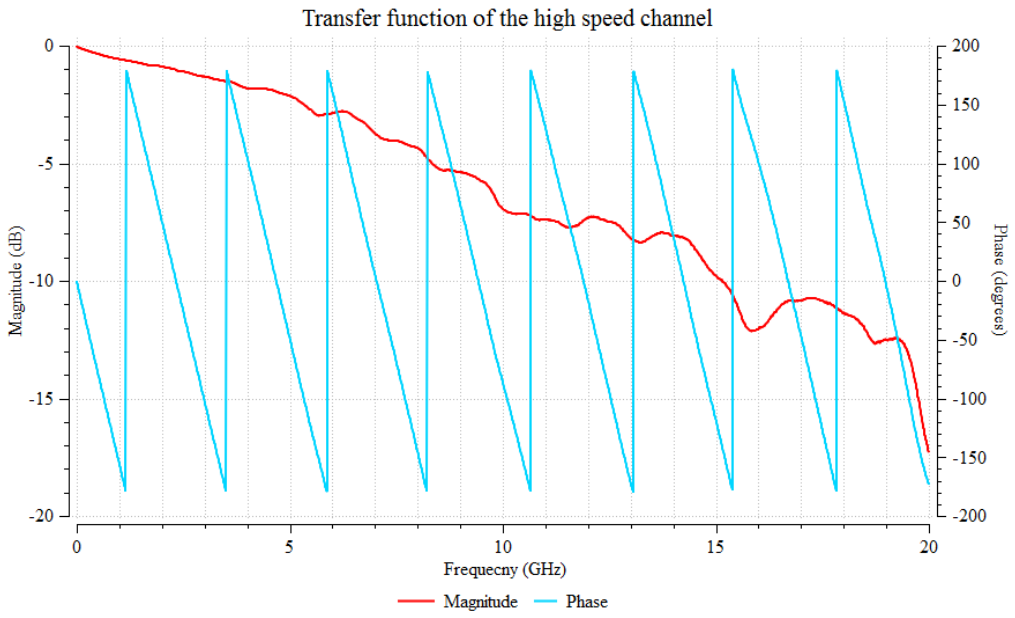

Figure 2.4. Magnitude and Phase of a High-Speed Link Path Transfer Function

The DHT-based causality enforcement algorithm reconstructing the minimal phase from the magnitude was applied. Figure 2.5 shows the nonlinear part of the phase of the transfer function before and after causality enforcement.

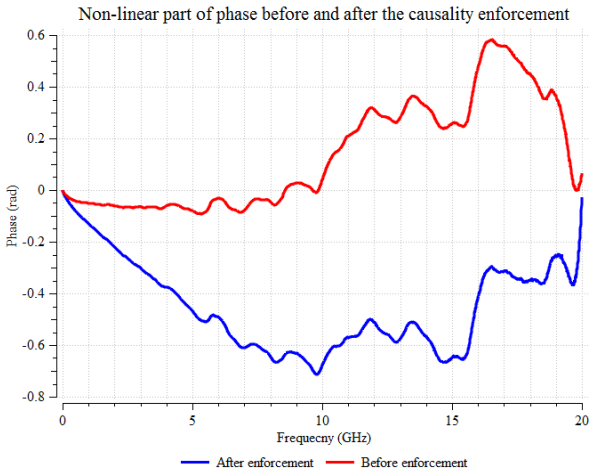

Figure 2.5. Nonlinear Phase before/after DHT-Based Causality Enforcement

Figure 2.6 shows impulse responses before and after the causality enforcement.

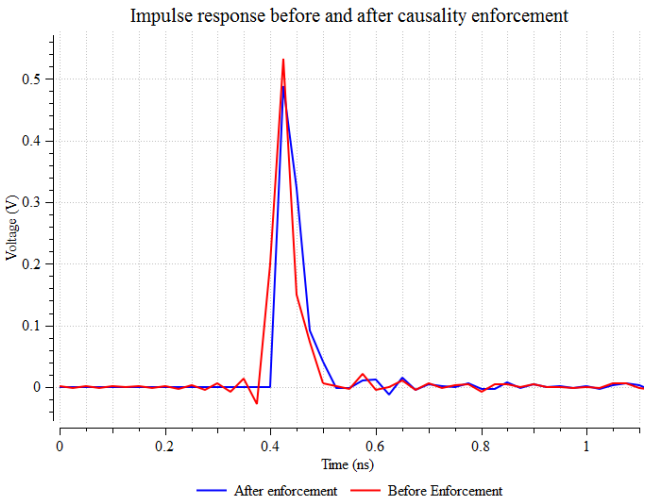

Figure 2.6. Impulse Responses before/after DHT-Based Causality Enforcement

This method uses the discrete Fourier transform, and therefore enforces causality in the time domain points corresponding to the given frequency domain sample points. That implies that an impulse response obtained from the frequency domain transfer function using IFFT will be perfectly causal. However, since DHT enforces causality and not delay causality, the data after enforcement has to be modified to return the delay portion of the phase. That will shift the impulse response and if the delay value is not divisible by the time step, non-causal ripples may appear before the delay. There are two possible solutions for this issue. If the delay is approximated by the closest value that is divisible by the step response, the ripples will be gone. Another similar solution is to return the delay in time domain by shifting the impulse response and then perform FFT to obtain the final transfer function.

The DHT-based causality enforcement approach has several major advantages over the approaches discussed in the previous sections. First of all, it provides a way to directly deal with the discrete, band-limited data and removes the problem of singularity (39) in the integral calculation. Second, frequency domain methods of causality enforcement from the previous sections do not guarantee a perfectly causal time domain response if it is constructed from the causality enforced frequency domain channel characterization using IFFT. However, as shown above, the DHT-based method provides a 100% causal function in the time domain. In addition, this is a much more efficient algorithm. For a frequency domain function sampled in N frequency points, the time of causality enforcement using the Hilbert integral is proportional to N^2 or to N^2M if the definition with M subtractions is used. At the same time, the DHT-based approach is proportional to $N \log N$, which is much faster. And finally, this method is much easier to implement since FFT and IFFT are readily available functions that do not need to be reimplemented.

2.4. CAUSALITY ENFORCEMENT APPLICATION EXAMPLES

This section illustrates the importance of using causality enforcement and provides examples of the algorithms described previously. It is often impossible to measure the link path of interest directly. In this case, the following technique is applied. Additional fixtures are attached to the system of interest which can be measured

individually, then the entire system with fixtures is measured, and finally the mathematical procedure is applied to compensate for the fixtures. The mathematical procedure of removing the effects of the known part of the system is called de-embedding. There are a lot of different algorithms for de-embedding. One of the current popular approaches is the 2X fixture de-embedding procedure [14]. This approach uses S-parameters complex value matrix arithmetic and is quite sensitive to the quality of the input data. This section illustrates how causality enforcement improves accuracy of the fixture de-embedding procedure result.

The 2X fixture de-embedding procedure consists of two main steps. First, measured S-parameters of the 2X structure are mathematically processed to obtain S-parameters of the left and right 1X fixtures. Then these fixtures are mathematically de-embedded from the measured S-parameters of the total structure to obtain the DUT's frequency domain characteristics. To demonstrate the importance of causality enforcement, S-parameters of the 2X structure were modified to add some artificial non-causal noise. To do that, random noise uniformly distributed over the interval $[-0.05, 0.05]$ was added to the through components of the fixture's transfer function. Figure 2.7 illustrates that the difference in the phase before extraction of its linear part is almost unnoticeable. However, the nonlinear part of phase shown in Figure 2.8 has a large deviation which, as it will be demonstrated later, has a big impact on the time domain simulation result.

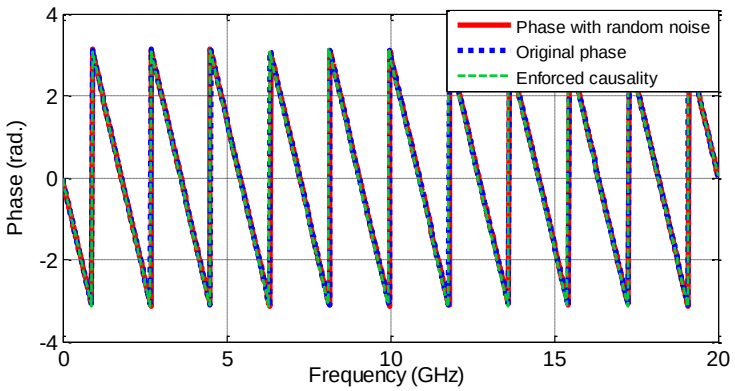

Figure 2.7. Total Phase of the 2X Structure without the Noise, with the Noise, and after the Causality Enforcement

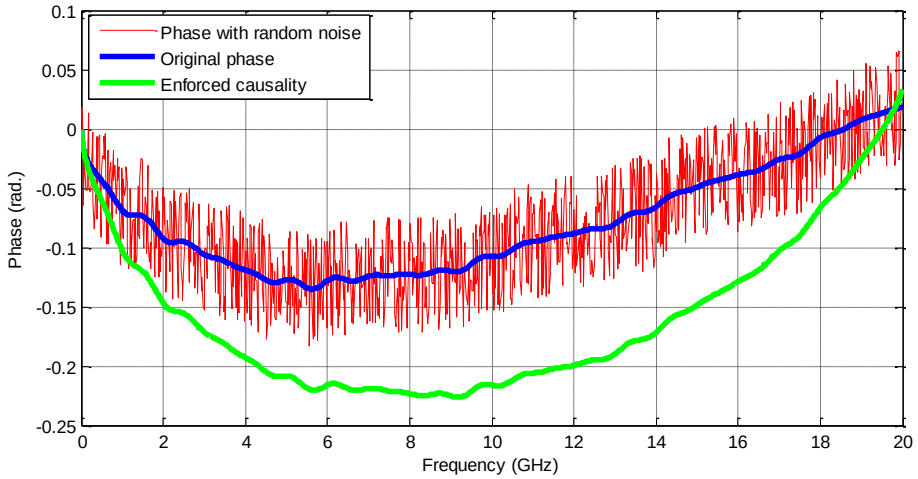

Figure 2.8. Nonlinear Part of the Phase of the 2X Structure without the Noise, with the Noise, and after Causality Enforcement

The original data, noisy data, and the data after causality enforcement were each used to obtain the 1X fixture and the DUT. Figure 2.9 and Figure 2.10 show the magnitude and total phase of S_{21} and S_{11} of the extracted DUT for all the cases. For the single-ended through simulation, the transfer function is equal to $\frac{1}{2}S_{21}$.

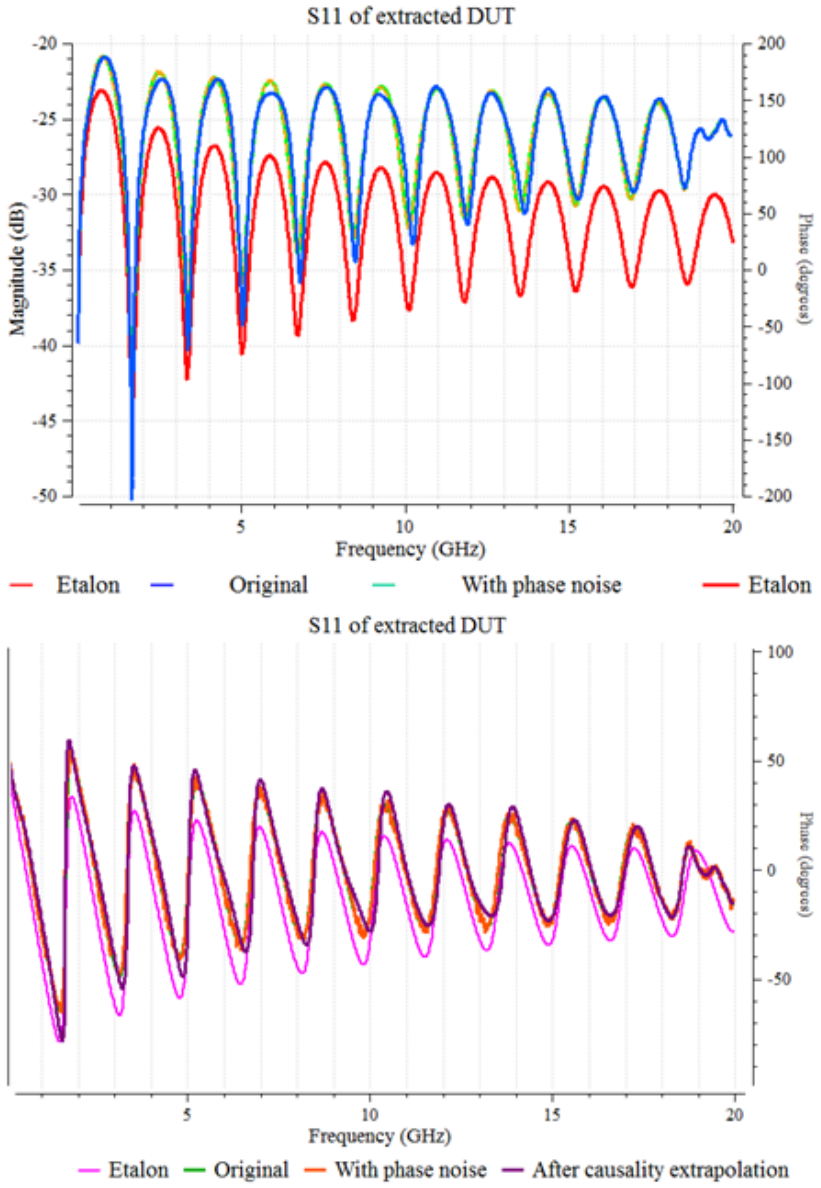

Figure 2.9. Magnitude and Total Phase of the Extracted DUT S_{11}

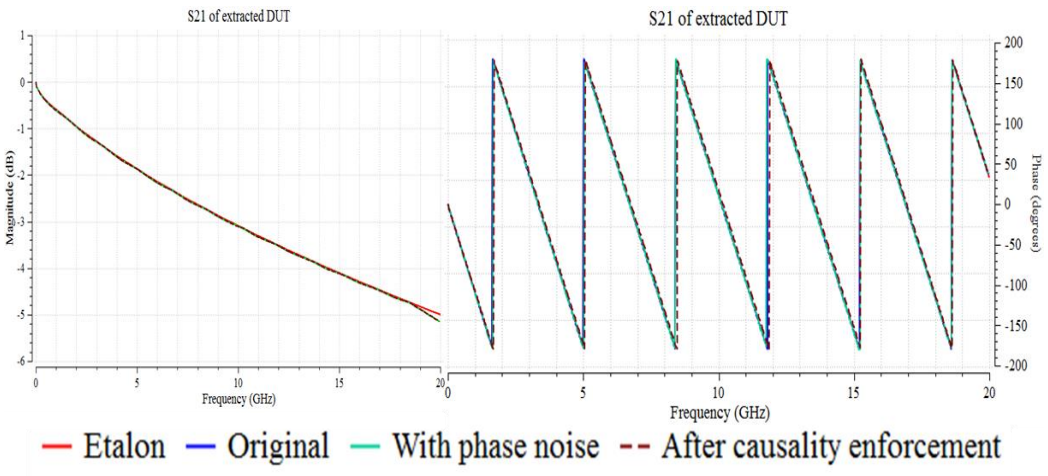

Figure 2.10. Magnitude and Total Phase of the Extracted DUT S_{21}

The difference in S_{21} appears to be relatively small until a closer look at the nonlinear part of the phase is taken. Figure 2.11 shows a significant difference in the non-linear part of the phase of the obtained results.

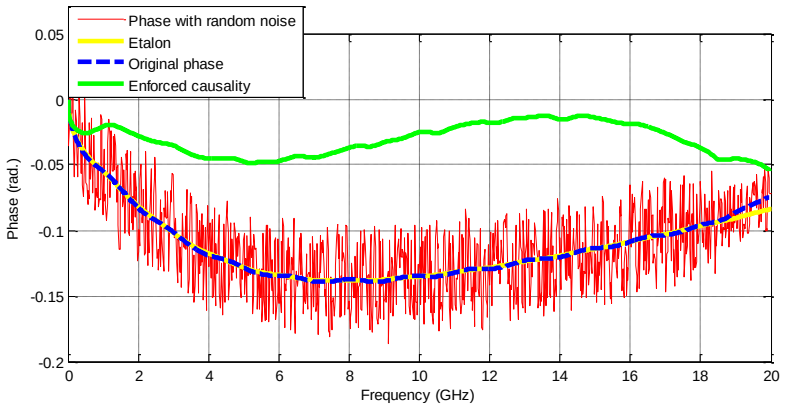

Figure 2.11. Nonlinear Part of the Phase of DUT S_{21}

To show the effect of the noisy and non-causal, nonlinear phase on the time domain simulation, the PRBS-15 pattern was used in the transient simulation with a 26 Gbps data rate and 20 ps rise/fall time to generate an eye diagram using all three

extracted DUTs as well as the etalon DUT obtained by a direct measurement. Figure 2.12 shows these eye diagrams.

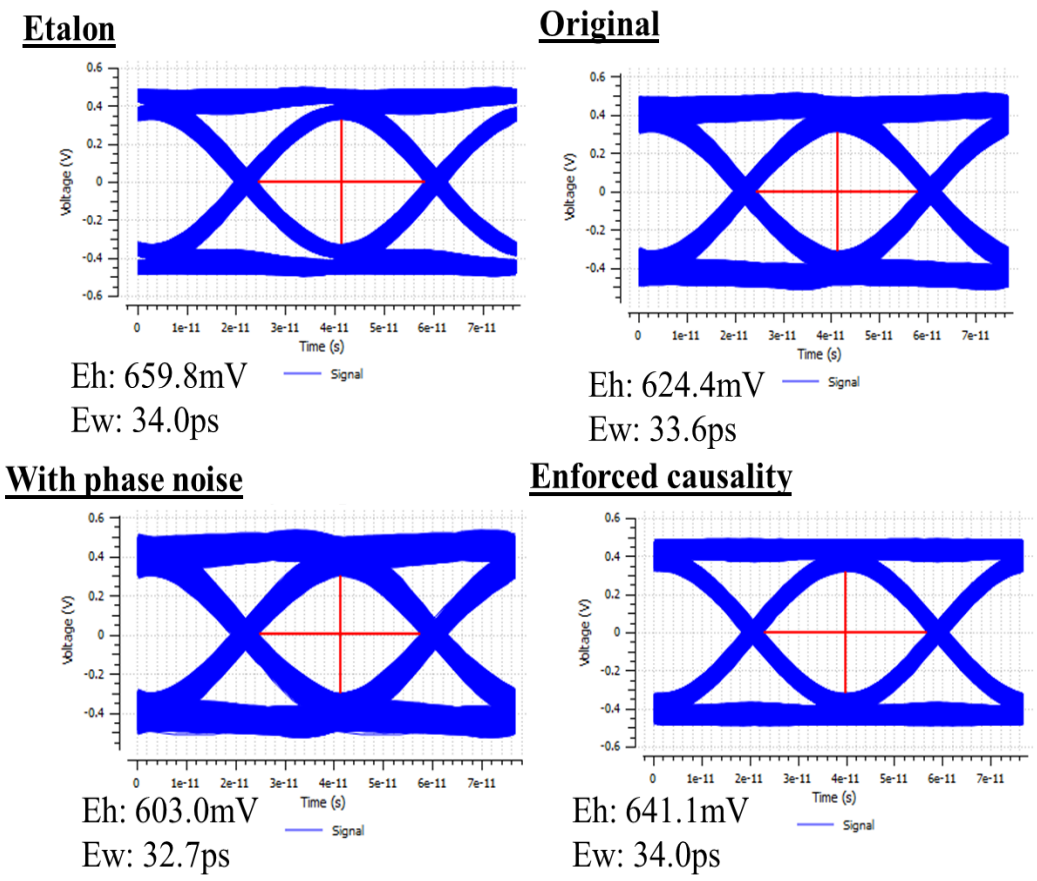

Figure 2.12. Comparison of the Transient Simulation Results of a DUT Extracted Using Measured 2X Structure, Noisy 2X Structure, and 2X Structure with Causality Enforcement

The noisy data shows significantly more pessimistic channel estimation while the causal data most closely matches that of the etalon DUT, even better than the original measured 2X structure before causality enforcement. Therefore, causality enforcement is an extremely useful technique to ensure the validity of the frequency domain data and quality of the time domain simulations. It can also be noted that it provides an effective method to clean the noise in the phase.

3. TIME DOMAIN METHOD FOR CHECKING AND ENFORCING DELAY CAUSALITY

Delay causality has to be enforced before the system model is used for a simulation to ensure valid and accurate results. The previous chapter describes a methodology for checking and enforcing causality using frequency domain system characterization. However, some simulation methodologies use impulse or step response as system characterization input. Then, the response of a system for a long input wave is obtained by convolving the impulse response with the input. Frequency domain causality enforcement methods are not the best choice for such simulation techniques as they will require additional computation time to convert data between time and frequency domains and will also introduce extra numerical errors in these transforms. Therefore, the technique for enforcing causality directly for an impulse response is necessary. This chapter gives a detailed analysis of such an approach.

3.1. CAUSALITY ENFORCEMENT FOR IMPULSE RESPONSE

This section describes a method of transforming a non-causal impulse response function in time domain to make it causal and the changes applied to the corresponding transfer function in frequency domain.

3.1.1. Time Domain Procedure for Enforcing Causality of Impulse Response.

Let $h(t)$ be an impulse response of a physical system with delay $\tau > 0$. The function $h(t)$ can be represented as a sum of odd and even functions regarding $t = \tau$:

$$h(t) = h_e(t) + h_o(t), \tag{68}$$

where:

$$h_e(t) = \frac{h(t)+h(t-\tau)}{2}, \tag{69}$$

$$h_o(t) = \frac{h(t)-h(t-\tau)}{2}. \quad (70)$$

Then, the modified impulse response function $\hat{h}(t)$ is defined as:

$$\hat{h}(t) = h_e(t) + sign(t-\tau)h_e(t). \quad (71)$$

This modification is equivalent to the following procedure: take the part of the impulse response before the delay, add its mirror image regarding the delay point to the part after the delay, and then set the part before the delay to zero. Figure 3.1 shows this time domain procedure.

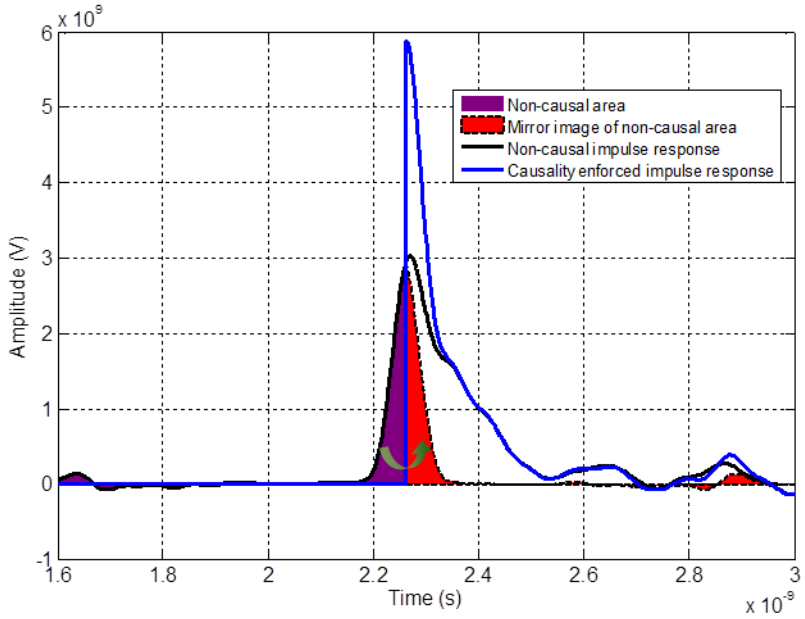

Figure 3.1. Time Domain Causality Enforcement Procedure

The modified function $\hat{h}(t)$ is a delay causal function, since for $t < \tau$:

$$\hat{h}(t) = h_e(t) + sign(t-\tau)h_e(t) = h_e(t) - h_e(t) = 0. \quad (72)$$

3.1.2. Frequency Domain Equivalence for Time Domain Enforcement.

This section describes the changes to the corresponding transfer function in the frequency domain related to the steps of the time domain enforcement algorithm.

Table 3.1 shows the parallel steps. Therefore, it is shown that the time domain causality enforcement algorithm is equivalent to the frequency domain causality enforcement using Kramers-Kronig relations between the real and imaginary parts of the transfer function.

Table 3.1. Time Domain Causality Enforcement and Its Frequency Domain Equivalence

Time Domain	**Frequency Domain**
Shift the impulse response $h(t)$ to the left by τ to obtain $h(t-\tau)$	Extract delay: $H'(\omega) = H(\omega)e^{-j\omega\tau}$
Represent the shifted impulse response as a sum of odd and even functions. $h(t-\tau) = \frac{h(t-\tau)+h(\tau-t)}{2} + \frac{h(t-\tau)-h(\tau-t)}{2}$	Represent the transfer function with the extracted delay as the sum of the real and imaginary parts (note the even part of the impulse response corresponds to the real part of the transfer function and the odd part corresponds to the imaginary []) $H'(\omega) = Re'(\omega) + jIm'(\omega)$
Remove the odd part from the shifted impulse response.	Remove the imaginary part from the transfer function with extracted delay.
Calculate the new odd part of the impulse response as $sign(t-\tau)h_e(t)$	Multiplication on $sign(t)$ in time domain corresponds to the Hilbert transform in the frequency domain. Calculate the imaginary part of the transfer function with extracted delay as the Hilbert transform of its real part: $Im'(\omega) = -\mathbb{H}\{Re'\}(\omega)$

Table 3.2. Time Domain Causality Enforcement and Its Frequency Domain Equivalence (cont.)

Shift the modified impulse response by τ on the right side: $\hat{h}(t) = \frac{h(t-\tau)+h(2\tau-t)}{2} + \frac{h(t-\tau)-sign(t-\tau)h(2\tau-t)}{2}$	Return the delay for the modified transfer function: $\widehat{H}(\omega) = [Re'(\omega) - \mathbb{H}\{Re'\}(\omega)]e^{j\omega\tau}$

3.2. CAUSALITY ENFORCEMENT FOR VECTOR FITTING BASED SIMULATION

3.2.1. Vector Fitting Approximation of Transfer Function. Frequency domain system characterization is usually obtained by measurements and/or simulations. Most of the time the result is tabulated data at certain frequency samples. Often it is much more beneficial to approximate this data with an analytical model. Physical models of electrical systems suggest that the most suitable class of functions to describe such models analytically is a class of rational functions. There are several reasons to prefer the rational functions: the result models are causal (not necessarily delay causal), passivity can be enforced at the construction stage, channel characterization can be analytically converted to the time domain, and finally, a corresponding circuit model can be generated to be used in further analysis and simulations. Thus, the tabulated transfer function can be approximated by a rational function with complex poles $p_1, p_2, \dots, p_n$ and complex residues $q_1, q_2, \dots, q_n$:

$$H(j\omega) \approx \sum_{i=1}^{n} \frac{q_i}{j\omega - p_i}. \tag{73}$$

The algorithm of vector fitting developed in [15] and [6] provides a way to construct such a representation. The corresponding impulse response can be obtained analytically and can be represented as the following sum:

$$h(t) \approx \sum_{i=1}^{n} q_i e^{p_i t}\ . \tag{74}$$

One of many applications of vector fitting is efficiently calculating the output of an electrical linear network.

3.2.2. Semi-Analytical Recursive Convolution. Channel response is obtained by convolving the impulse response with the input signal. Let $r(t)$ be the input signal and $h(t)$ be the impulse response of the considered system. Then, the channel response with time domain enforced causality $y(t)$ for $t \in [0, T]$ can be calculated by the following formula:

$$y(t) = \int_0^t h(t-s)r(s)ds. \tag{75}$$

If both the impulse response and input signal are given as tabulated data for discrete time samples, then the straightforward approach of calculating convolution as an integral (75) has a calculation time that depends on the length of the input signal as a quadratic function, which makes it computationally inefficient. However, once impulse response is represented by (74), the recursive semi-analytical algorithm for convolution proposed in [16] can be used. For this approach (75) can be rewritten as:

$$y(t) = \sum_{i=1}^{n} q_i \int_0^t e^{p_i(t-s)}r(s)ds = \sum_{i=1}^{n} q_i \; u_i(t). \tag{76}$$

Then, to calculate a particular value of $y(t_k)$, each integral $u_i(t_k)$ under the summation can be expressed in the recursive formula:

$$u_i(t_k) = \int_0^{t_{k-1}} e^{p_i(t_k-s)}r(s)ds + \int_{t_{k-1}}^{t_k} e^{p_i(t_k-s)}r(s)ds = e^{p_i\Delta t}u_i(t_{k-1}) + \delta_i^k. \tag{77}$$

Integrals δ_i^k can be calculated numerically, but that is an extra calculation burden and a source of a potentially large numerical error. Instead of calculating them numerically, they can be calculated analytically if the input signal is approximated by linear interpolation. On the interval $[t_{k-1}, t_k]$ the following approximation is used:

$$r(s) \approx r(t_{k-1}) + \frac{s - t_{k-1}}{t_k - t_{k-1}}\big(r(t_k) - r(t_{k-1})\big). \tag{78}$$

Using (78) the following formula can be obtained:

$$\delta_i^k = \frac{1}{p_i}\left[r(t_k)\left(\frac{e^{p_i\Delta t}-1}{p_i\Delta t} - 1\right) - r(t_{k-1})\left(\frac{e^{p_i\Delta t}-1}{p_i\Delta t} - e^{p_i\Delta t}\right)\right]. \tag{79}$$

Assuming that $u_i(0) = 0$, all the values of $y(t)$ can be recursively calculated. This recursive, semi-analytical algorithm for the convolution achieves linear asymptotic complexity. Note that while this algorithm is asymptotically much better than the FFT approach, it does not necessarily beat it in practice. For input signals containing N samples and vector fitting with M poles, Table 3.3 shows the comparison of the asymptotic complexity of different approaches. Recursive convolution is dominant for the very large N. However, for $N < 2^M$, FFT is a more efficient approach. Typical values for M are around 100, which makes it unlikely for N to reach that threshold. However, the benefit of using recursive convolution is that it automatically enforces passivity and causality (not delay causality) for the model.

Table 3.3. Asymptotic Complexity of Different Transient Simulation Algorithms

	Naïve Convolution	FFT	Vector Fitting and Recursive Convolution
Asymptotic complexity	$O(N^2)$	$O(NlogN)$	$O(MN)$

3.2.3. Stable Recursive Convolution with Causality Enforcement. To be able to use the recursive convolution approach together with the time domain causality enforcement described earlier, modifications to the algorithm have to be made. This section derives the modified algorithm. Let $r(t)$ be an input signal and $\hat{h}(t)$ be the modified impulse response (71). Then, the channel response with time domain enforced causality $y(t)$ for $t \in [0, T]$ can be calculated by the following formula:

$$y(t) = \int_0^t \hat{h}(t-s)r(s)ds. \tag{80}$$

If impulse response $h(t)$ is given by (74), then the modified impulse response will be given as the following:

$$\begin{gathered} \hat{h}(t) = h_1(t) + h_2(t) \\ h_1(t) = \begin{cases} 0, & t < \tau \\ \sum_{i=1}^{n} q_i e^{p_i t}, & t \geq \tau \end{cases} \\ h_2(t) = \begin{cases} 0, & t < \tau \\ \sum_{i=1}^{n} q_i e^{p_i(2\tau - t)}, & \tau \leq t \leq 2\tau. \\ 0, & t > 2\tau \end{cases} \end{gathered} \tag{81}$$

For efficient numerical calculations it is important to obtain the recursive formula for (80). The values of the input signal $r(t)$ are given at the discrete points $t_k = k\Delta t, k = 0,1, \dots, N$ and $\Delta t = \frac{T}{N}$. Then channel response at $t = t_k$ can be written as the following:

$$\begin{gathered} y_k = \int_0^t \hat{h}(t-s)r(s)ds = \int_0^t \big(h_1(t) + h_2(t)\big)r(s)ds = \\ \sum_{i=1}^{n} q_i \big(A_{i,k} + B_{i,k}\big), \end{gathered} \tag{82}$$

where:

$$A_{i,k} = \int_0^{t_{k-k_0}} e^{p_i(t_k-s)} r(s)ds\,, \quad t_{k_0} = \tau \tag{83}$$

$$B_{i,k} = \int_{t_{k-2k_0}}^{t_{k-k_0}} e^{p_i\left(t_{2k_0}+s-t_k\right)} r(s)ds. \tag{84}$$

Similar to the recursive convolution approach without causality enforcement, a recursive formula for $A_{i,k}$ can be obtained:

$$A_{i,k} = \int_0^{t_{k-k_0}} e^{p_i(t_k-s)} r(s)ds$$

$$= \int_0^{t_{(k-1)-k_0}} e^{p_i(t_k-s)} r(s)ds \; + \int_{t_{(k-1)-k_0}}^{t_{k-k_0}} e^{p_i(t_k-s)} r(s)ds$$

$$A_{i,k} = e^{p_i\Delta t} A_{i,k-1} + \alpha_{i,k}, \tag{85}$$

where $k \geq k_0$, $A_{i,k_0} = 0$ and

$$\alpha_{i,k} = \int_{t_{(k-1)-k_0}}^{t_{k-k_0}} e^{p_i(t_k-s)} r(s)ds. \tag{86}$$

Integral (86) can be calculated by the same semi-analytical method as integral δ_i^k. The modified formula is:

$$\alpha_{i,k} = \frac{e^{p_i t_{k_0}}}{p_i}\left[r_{k-k_0}\left(\frac{e^{p_i\Delta t}-1}{p_i\Delta t} - 1\right) - r_{k-1-k_0}\left(\frac{e^{p_i\Delta t}-1}{p_i\Delta t} - e^{p_i\Delta t}\right)\right]. \tag{87}$$

Similarly, the recursive formula for $B_{i,k}$ can be obtained:

$$B_{i,k} = e^{-p_i \Delta t} B_{i,k-1} + \beta_{i,k}^1 - \beta_{i,k}^2, \tag{88}$$

where $k \geq k_0$, $B_{i,k_0} = 0$ and

$$\begin{aligned} \beta_{i,k}^1 &= \int_{t_{k-1-k_0}}^{t_{k-k_0}} e^{p_i\left(t_{2k_0}-(t_k-s)\right)} r(s) ds \\ \beta_{i,k}^2 &= \int_{t_{k-1-2k_0}}^{t_{k-2k_0}} e^{p_i\left(t_{2k_0}-(t_k-s)\right)} r(s) ds. \end{aligned} \tag{89}$$

However, calculations of $B_{i,k}$ based on (88) will be numerically unstable. Vector fitting guarantees that poles have a negative real part, and so $-p_i$ will have a positive real part and then $e^{-p_i \Delta t}$ will be a very large number and all numerical errors will be greatly amplified. Figure 3.2 shows the instability of the algorithm, based on (88).

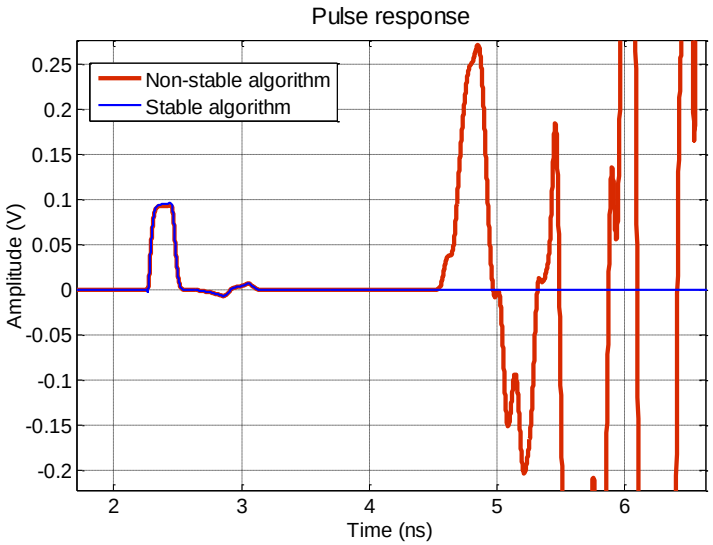

Figure 3.2. Instability Issue of the Recursive Convolution for Causality Enforced Impulse Response

One can see that instability occurs at the time point of the double delay because it is the point where coefficient $\beta_{i,k}^2$ starts being used. Ideally, it would balance $\beta_{i,k}^1$ and the formula would work. However, a numerical error in calculations of these coefficients becomes majorly amplified by the $e^{-p_i\Delta t}$ term (which is very large because $-p_i$ has a positive real part) and leads to tremendous instability. To avoid this issue, making backward calculations in time is suggested: recursively calculate $B_{i,k}$ from $B_{i,k+1}$. For such an algorithm, (88) can be modified:

$$B_{i,k} = e^{p_i\Delta t}\left(B_{i,k+1} - \beta_{i,k+1}^1 + \beta_{i,k+1}^2\right). \tag{90}$$

Figure 3.2 illustrates that this algorithm does not have an instability problem. Analogous to (87), $\beta_{i,k}^1$ and $\beta_{i,k}^1$ can be calculated semi-analytically using a piecewise linear approximation of the input signal:

$$\begin{aligned}\beta_{i,k}^1 = \frac{e^{p_i(t_{k_0}-\Delta t)}}{p_i}\Bigg[&r_{k-1-k_0}\left(\frac{e^{p_i\Delta t}-1}{p_i\Delta t}-1\right)\\ &- r_{k-k_0}\left(\frac{e^{p_i\Delta t}-1}{p_i\Delta t}-e^{p_i\Delta t}\right)\Bigg]\end{aligned} \tag{91}$$

$$\beta_{i,k}^2 = \frac{e^{-p_i\Delta t}}{p_i}\left[r_{k-1-2k_0}\left(\frac{e^{p_i\Delta t}-1}{p_i\Delta t}-1\right) - r_{k-2k_0}\left(\frac{e^{p_i\Delta t}-1}{p_i\Delta t}-e^{p_i\Delta t}\right)\right].$$

For the numerical calculation of the iterative algorithm based on (91), it is necessary to calculate the last point B_N:

$$B_{i,N} = \int_{t_{N-2k_0}}^{t_{N-k_0}} e^{p_i(t_{2k_0}+s-t_N)}r(s)ds = \sum_{m=0}^{k_0-1}\int_{t_{N+m-2k_0}}^{t_{N+(m+1)-k_0}} e^{p_i(t_{2k_0}+s-t_N)}r(s)ds$$

$$B_{i,N} = \sum_{m=0}^{k_0-1}\frac{e^{p_i(t_{N+m}-t_N)}}{p_i}\left[r_{N+m-k_0}\left(\frac{e^{p_i\Delta t}-1}{p_i\Delta t}-1\right) - r_{N+(m+1)-k_0}\left(\frac{e^{p_i\Delta t}-1}{p_i\Delta t}-e^{p_i\Delta t}\right)\right].$$

3.2.4. Application Example and Results Comparison. The following application example illustrates the proposed recursive convolution algorithm with time domain causality enforcement. S-parameters of the stripline structure were measured and used to simulate the response of a 10 Gbps pulse with a 30 ps rise time. For a matched channel transfer function of a through channel, it is equal to the S21 component of the channel's S-parameters. Figure 3.3 shows the magnitude and phase of the measured S21 component.

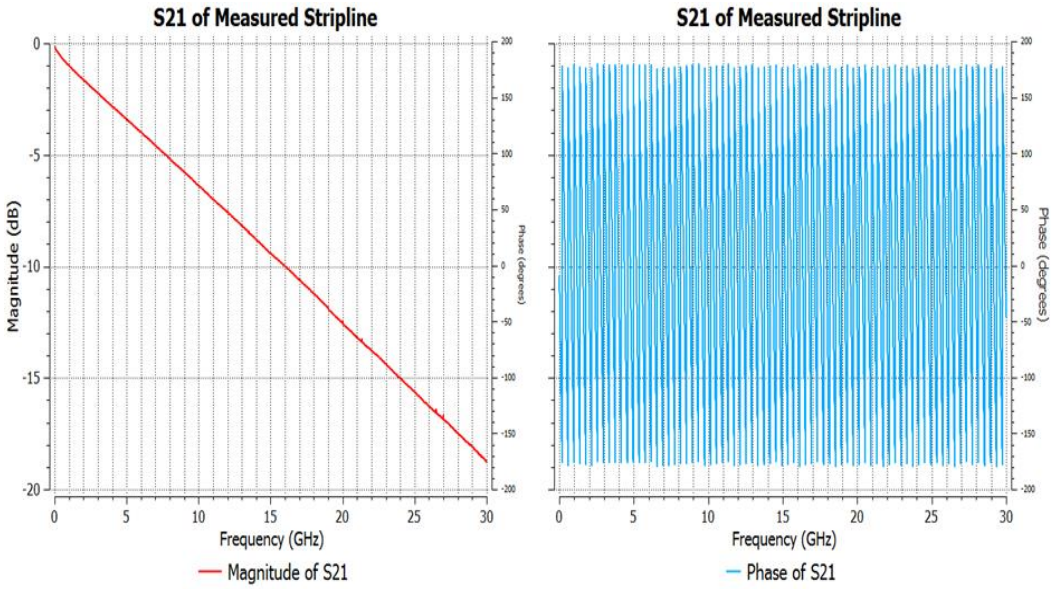

Figure 3.3. Measured Transfer Function of the Stripline

S-parameters of the real system must be causal; however, because of measurement errors they still have to be checked before use. For this example, less than 0.1% of the pulse response energy has come before the delay, thus this data can be considered causal. Further, the transfer function was multiplied on $e^{j\alpha\sqrt{\omega}}$, where α was a random variable with values evenly distributed over the interval $[-0.1, 0.1]$, which introduced some random nonlinear distortion to the transfer function's phase. Since magnitude was not modified and causal functions should satisfy Kramer-Kronig relations between magnitude and phase, the modified S-parameters become non-causal. Figure 3.4

shows the real and imaginary part of the transfer function after the phase noise introduction.

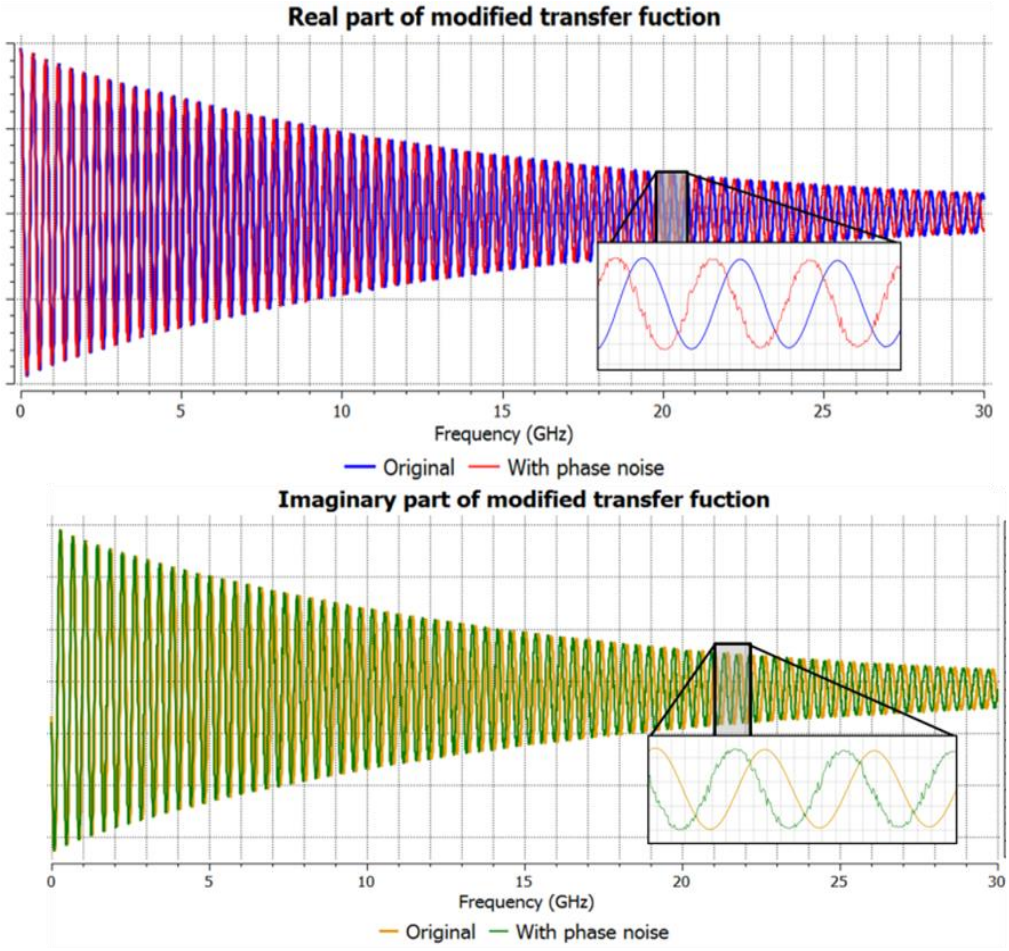

Figure 3.4. Measured Transfer Function of the Stripline with Additional Phase Noise

Then, the modified S-parameters were used to obtain the pulse response both with and without time domain causality enforcement. Figure 3.5 shows the original causal pulse response, pulse response of the modified non-causal S-parameters, and pulse response of the modified S-parameters with enforced causality.

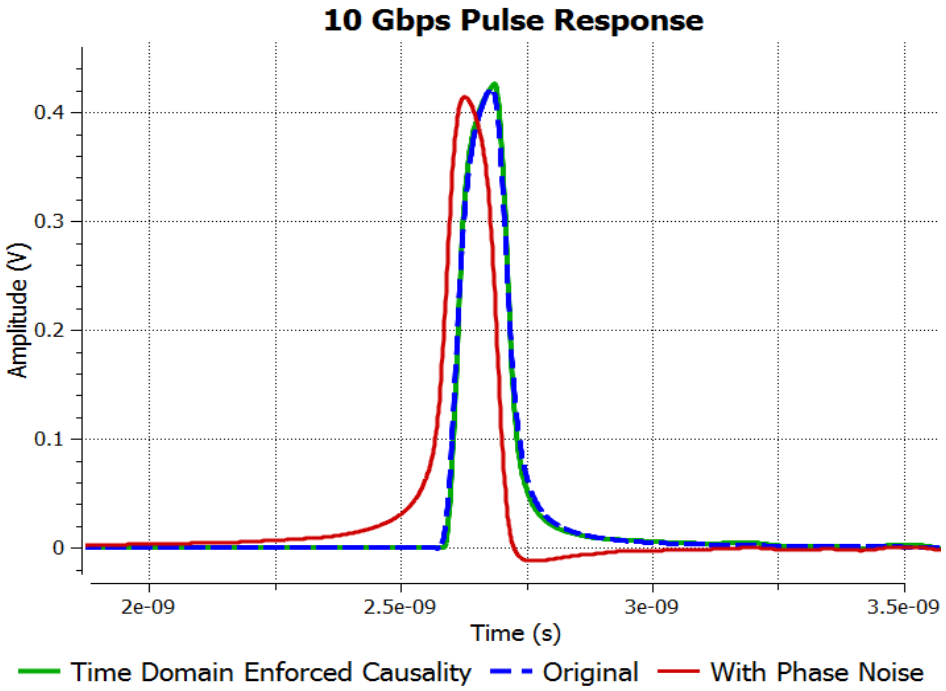

Figure 3.5. Comparison of Pulse Responses with and without Causality Enforcement

4. SYSTEM LEVEL MODELING QUALITY

Existing measurement techniques have numerous limitations. Obtained data is noisy, discrete, and band-limited while the mathematical model of a linear network describes a system analytically and continuously on the infinite frequency band. Because of this, the result of simulations is always just an approximation. Since systems become more sensitive at the high frequencies, these errors become much larger as well. As high-speed data links keep evolving, data rates keep increasing and it becomes extremely important to improve the accuracy of the models and simulation procedures. While any limitations and deviations in the data decrease the accuracy, it can still be acceptable as long as important assumptions of the simulation procedure itself are not violated. If this happens, the output of such simulation does not describe the system under test at all and relying on such data can lead to making wrong decisions. This section is dedicated to two such assumptions, shows the importance of not violating them, and proposes techniques for enforcing them on the data.

4.1. EXTRAPOLATION OF FREQUENCY DOMAIN DATA TO DC

Modern frequency domain measurement equipment cannot simultaneously cover high and low frequency ranges with good resolution and accuracy. For high-speed systems considered by signal integrity engineers, it is essential to capture the high-frequency behavior. It is very common to receive data that lacks several values next to DC and the DC point itself. However, many simulation techniques rely on the assumption that data starts from 0 Hz and has even frequency steps. One of the important examples is the Fast Fourier Transform (FFT) algorithm often used for transient simulations. Therefore, it becomes critical to extrapolate the data into the DC region before using it in the simulations. The technique proposed below allows doing such an extrapolation in a way that is compliant with the expected physical behavior.

For a transfer function of a linear electrical network $H(\omega) = Re(\omega) + jIm(\omega) = e^{-\rho(\omega)-j\varphi(\omega)}$, the following condition is true:

$$H(-\omega) = H^*(\omega), \tag{94}$$

which implies the following relations:

$$\begin{aligned} \rho(-\omega) = \rho(\omega) \;\; Re(-\omega) = Re(\omega) \\ \varphi(-\omega) = -\varphi(\omega) \;\; Im(-\omega) = -Im(\omega). \end{aligned} \tag{95}$$

Given that two first available data points and their corresponding values are ω_1, ω_2 and $H(\omega_1), H(\omega_2)$, the values at the corresponding negative frequency points are also known. Besides, (95) implies that $\varphi(0) = Im(0) = 0$. Therefore, extrapolation can be substituted by interpolation between the first given positive frequency and its opposite frequency point. Interpolation is a much more stable numerical algorithm and it controls the behavior as long as the values at certain points of the interpolated function are known. There can be several different ways to choose the interpolation technique. Below there is a specific practical approach for a linear electrical network transfer function extrapolation to DC:

$$\widetilde{Im}(\omega) = \frac{Im(\omega_1)\omega_2 - Im(\omega_2)\omega_1}{\omega_1^3\omega_2 - \omega_2^3\omega_1}(\omega^3 - \omega_1^2\omega) + \frac{Im(\omega_1)}{\omega_1}\omega. \tag{96}$$

If $|H(\omega_1)| > |H(\omega_2)|$:

$$\begin{aligned} \widetilde{Re}(\omega) = \frac{Re(\omega_1) - Re(\omega_2)}{\omega_1^2 - \omega_2^2}\omega^2 \\ + \left(Re(\omega_1) - \frac{Re(\omega_1) - Re(\omega_2)}{\omega_1^2 - \omega_2^2}\omega_1^2\right), \end{aligned} \tag{97}$$

else:

$$\tilde{\rho}(\omega) = \frac{\rho(\omega_2) - \rho(\omega_1)}{\omega_2 - \omega_1}\omega + \left(\rho(\omega_1) - \frac{\rho(\omega_2) - \rho(\omega_1)}{\omega_2 - \omega_1}\omega_1\right)$$
$$\widetilde{Re}(\omega) = \sqrt{[e^{\tilde{\rho}(\omega)}]^2 - \left[\widetilde{Im}(\omega)\right]^2}. \quad (98)$$

To illustrate the accuracy of the proposed extrapolation method, data containing a DC point was taken. The first five values were removed and the described extrapolation technique was applied. Figure 4.1 and Figure 4.2 show the comparison between the original and extrapolated values for the imaginary and real parts respectively. Extrapolation error at all the samples does not exceed 2%.

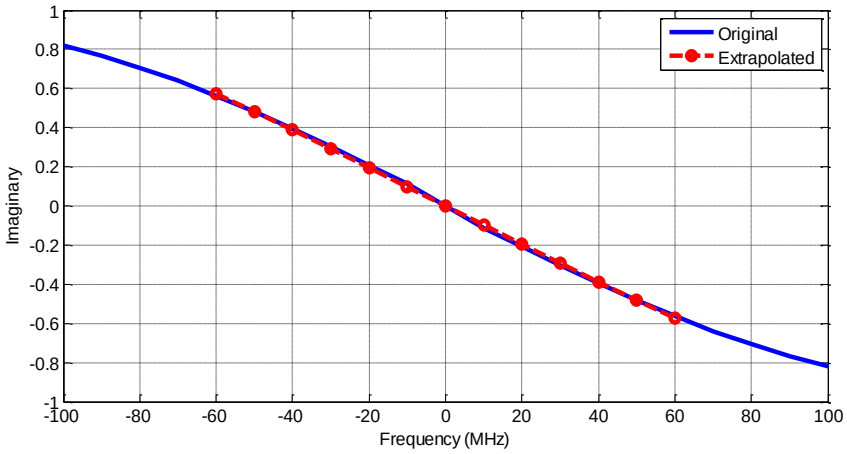

Figure 4.1. Original and Extrapolated Imaginary Part

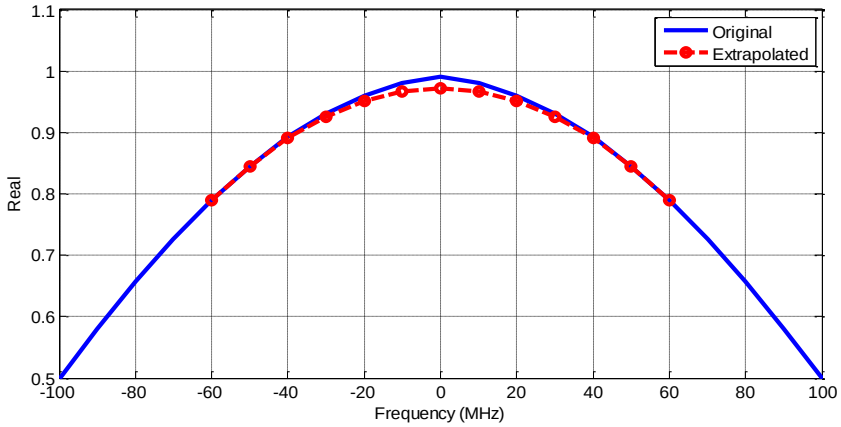

Figure 4.2. Original and Extrapolated Real Part

Figure 4.3 shows impulse responses obtained from the frequency domain data using the inverse Fast Fourier transform. The red curve was obtained using the original data that had the DC value. The blue curve was obtained using the same data, but without the first several low frequency points. Finally, the green curve was obtained from the data with missing low frequencies after the extrapolation technique was applied.

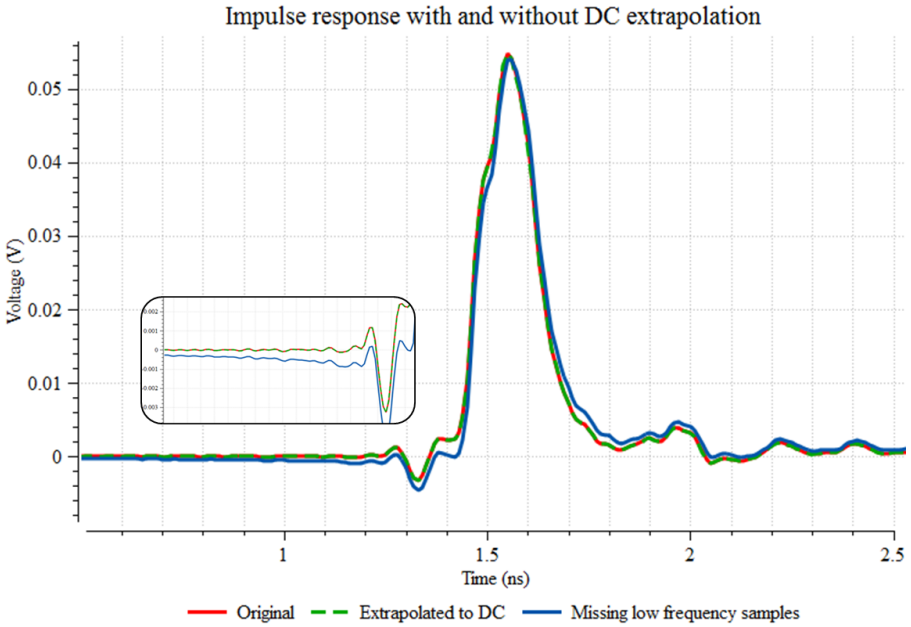

Figure 4.3. Impulse Responses of Data with and without DC Value

There are noticeable differences between the impulse responses. The response without the DC point has much bigger causality violations which can be seen in the zoomed-in area. These inaccuracies significantly add up for the long waveform simulation. On the other hand, it can also be seen that the impulse response after the extrapolation is very close to the original impulse response that was calculated using the data containing the DC point, showing the quality of the proposed technique.

To illustrate the effects of the missing DC samples on the time domain simulation, the following example was produces in FEMAS [17]. Figure 4.4 shows the magnitude of the measured transfer function of the fixture of a high-speed PCB.

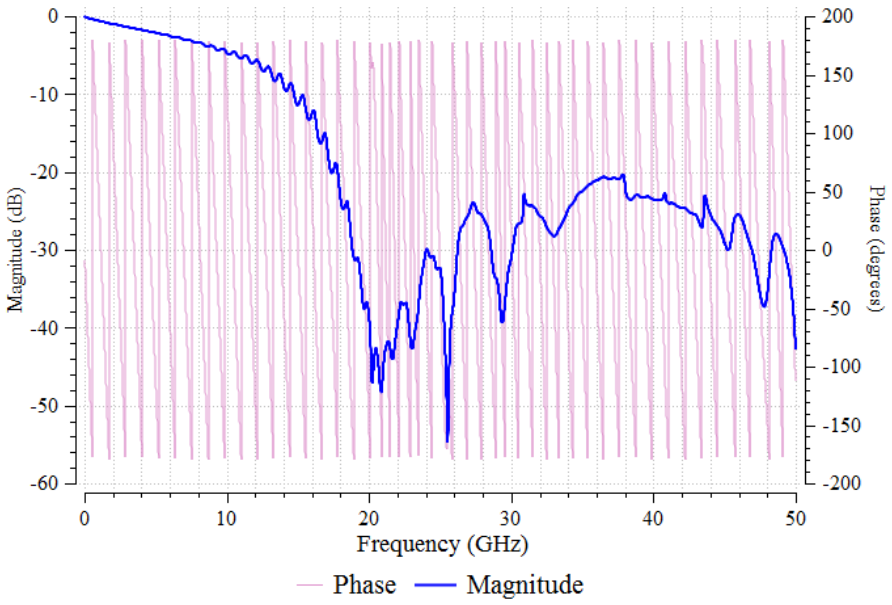

Figure 4.4. Measured Magnitude and Phase of the High-Speed PCB Fixture

It was used for a transient simulation of five repetitions of PRBS9, with a 10 Gbps bit rate and 30 ps rise/fall time. The results are shown below in the Figure 4.5.

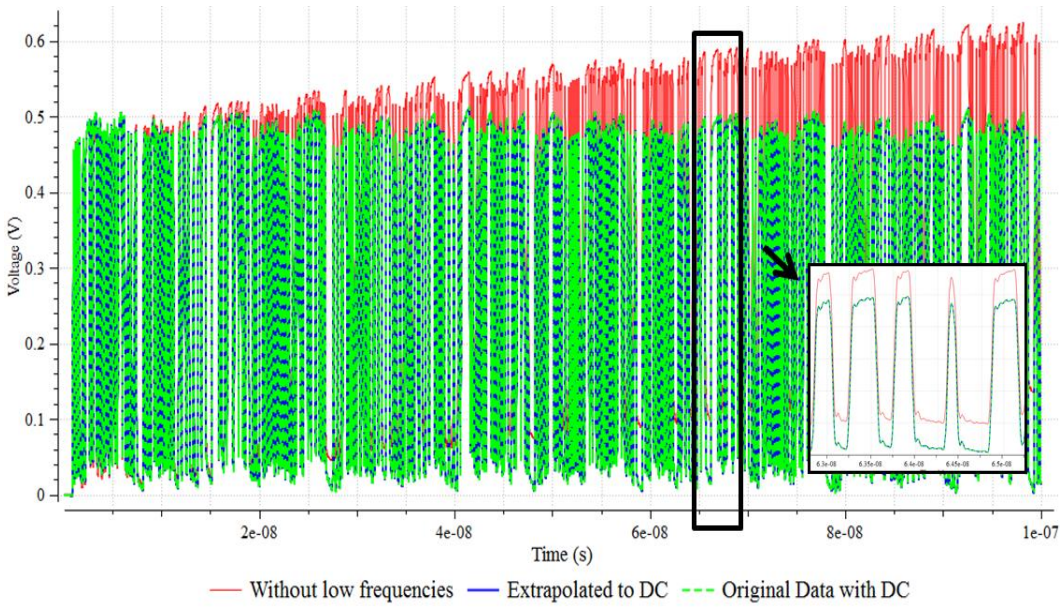

Figure 4.5. Effect of the Missing Low Frequency Samples on the Long Transient Simulation

It is clearly seen that the missing DC points create a big instability and inaccuracy of the final results, while the proposed DC extrapolation method restores the results to the original accurate values.

4.2. ACCURATE FREQUENCY DOMAIN INTERPOLATION TECHNIQUE

System-level simulation for signal integrity usually requires connecting together models of the various subparts. Different measurements and/or simulations might be a source of frequency characteristic data corresponding to those subparts. The frequency characteristics can be measured or simulated for different frequency samples. To obtain the whole system it is necessary to cascade the frequency characteristics corresponding to subparts of the model. Frequency characteristics can be cascaded only if they are given at the same frequency samples. Therefore, interpolation of such frequency responses is necessary to reduce the data to common frequency samples. Different interpolation methodologies can be used to reduce all frequency responses to the same frequency samples [18], [19]. However, not every methodology, even some very intuitive and widely used, provide an accurate, physically valid results. This section is dedicated to a

thorough analysis of such methods, their challenges and proposes an accurate interpolation method.

4.2.1. Naïve Linear Frequency Domain Interpolation. The simplest frequency domain interpolation method is a linear interpolation of the real and imaginary parts of the given frequency responses. Assume that the original frequency response $H(\omega)$ is given at frequency samples $\omega_1, \omega_2, \dots, \omega_N$ with the corresponding values $H_1, H_2, \dots, H_N, H_k = R_k + jI_k$. These values have to be interpolated at the frequency samples $\bar{\omega}_1, \bar{\omega}_2, \dots, \bar{\omega}_M$ to corresponding values $\bar{H}_1, \bar{H}_2, \dots, \bar{H}_N, \bar{H}_k = \bar{R}_k + j\bar{I}_k$. The linear interpolation of the real and imaginary parts of the transfer function can be done using the following formulas:

$$\begin{aligned} \bar{R}_i &= \frac{\bar{\omega}_i - \omega_{k+1}}{\omega_k - \omega_{k+1}} R_k + \frac{\bar{\omega}_i - \omega_k}{\omega_{k+1} - \omega_k} R_{k+1} \\ \bar{I}_i &= \frac{\bar{\omega}_i - \omega_{k+1}}{\omega_k - \omega_{k+1}} I_k + \frac{\bar{\omega}_i - \omega_k}{\omega_{k+1} - \omega_k} I_{k+1}, \end{aligned} \tag{99}$$

where $\bar{\omega}_i \in [\omega_k, \omega_{k+1}]$. The interpolation done using (99) can work well for short structures, but if the structure is long the interpolation can create artificial effects in the time domain. Linear interpolation using (99) was done for the frequency responses of a measured 3 m differential cable and differential 1.2 in microstrip with 2.4 mm SMA connectors and 6 in cables at each side. The detailed geometry model of the microstrip is shown in Figure 4.6. Figure 4.7 shows the magnitudes and phases of the frequency responses of the measured microstrip and 3 m cable.

Figure 4.6. Geometry Model of the Microstrip

The microstrip with connectors was measured up to 30 GHz and the 3 m cable was measured up to 14 GHz. The original frequency responses for both structures are given on frequency samples with a 10 MHz step. Interpolation was done for a 10.2 MHz frequency step (original frequency samples changed just by 2%).

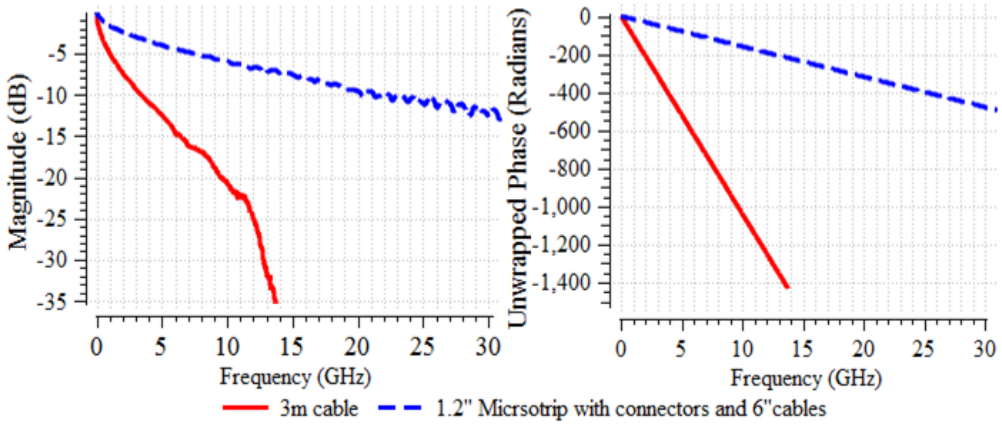

Figure 4.7. Magnitudes/Phases of SDD21 of the 3 m Cable and Microstrip

Effectively, it corresponds to the pulse/step responses with the rise/fall time equal to one time step. In the presented cases, the time step is equal to 35 ps for the 3 m cable and 18 ps for the microstrip. Figure 4.8 and Figure 4.9 demonstrate that even a small change in frequency step can cause artificial effects on the impulse response of a 3 m cable after interpolation.

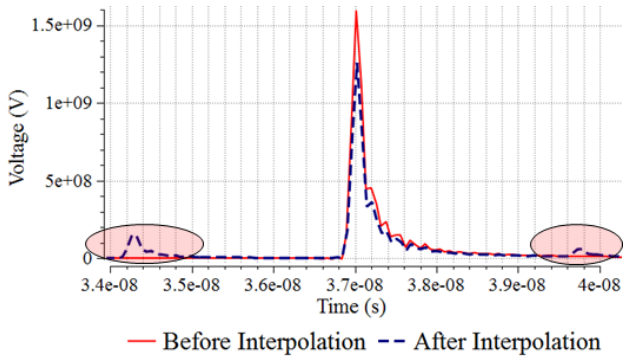

Figure 4.8. Impulse Response before and after Interpolation for the 3 m Cable

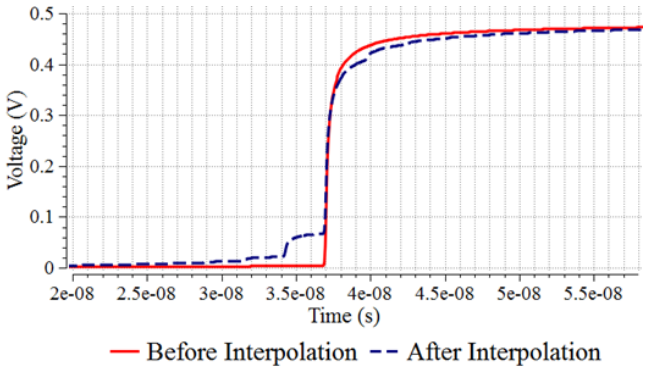

Figure 4.9. Step Response before and after Interpolation for the 3 m Cable

It can be seen that the energy of the impulse response was redistributed over the time interval which also caused the decrease of the amplitude of the main pulse. However, Figure 4.10 and Figure 4.11 show that the same effect is not observed for the microstrip. They show the impulse and step responses before and after interpolation for the microstrip, respectively. For this case, no distortion in time domain responses after the interpolations is observed.

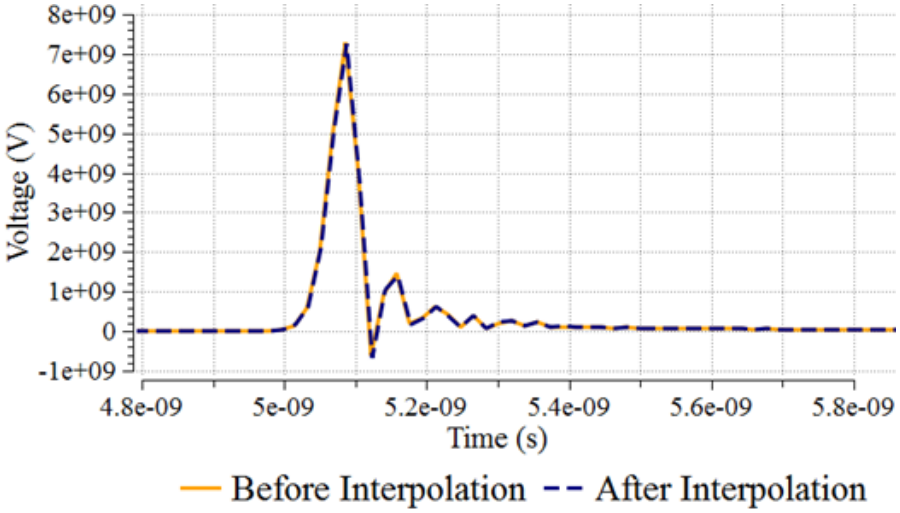

Figure 4.10. Impulse Responses before and after Interpolation for the Microstrip

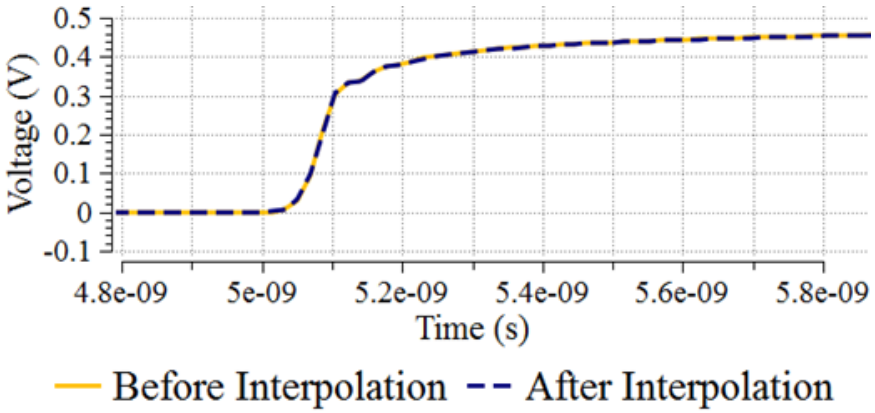

Figure 4.11. Step Responses before and after Interpolation for the Microstrip

The artifacts shown in Figure 4.8 and Figure 4.9 are related with the spectral leakage phenomena originated by the lack of coherence [20].

4.2.2. Artifacts after Frequency Domain Interpolation. To analyze the nature of the artifacts shown in Figure 4.8 and Figure 4.9, the magnitudes and phases of the frequency responses before and after interpolation need to be inspected. Figure 4.12 and Figure 4.13 show the magnitudes and phases of the original and interpolated frequency responses respectively for a 3 m cable.

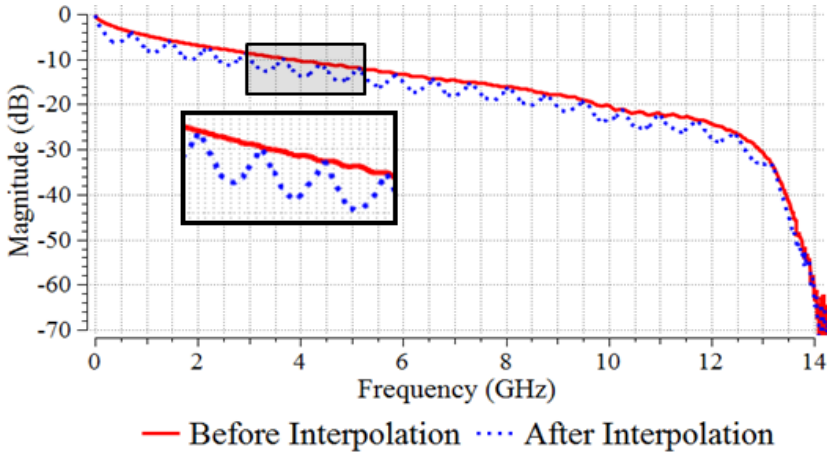

Figure 4.12. Magnitude of SDD21 of the 3 m Cable before and after Interpolation

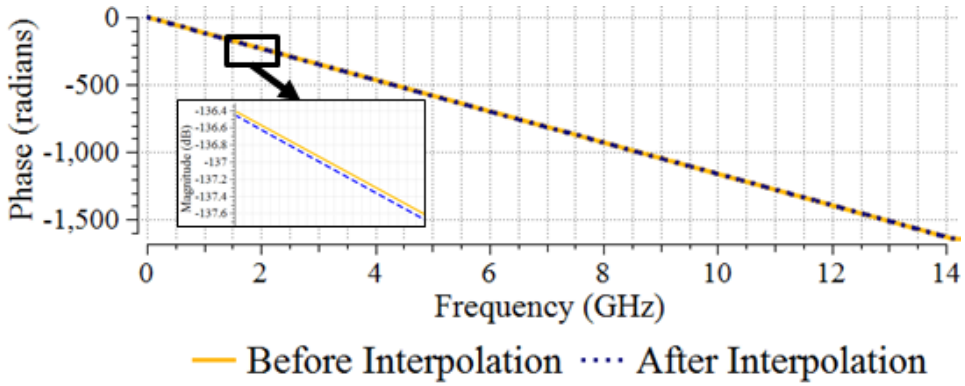

Figure 4.13. Phase of SDD21 of the 3 m Cable before and after Interpolation

Figure 4.12 and Figure 4.13 show that the magnitude interpolation is very inaccurate. The reason for the inaccuracy is the real and imaginary parts of the frequency responses for long structures are highly oscillated and the linear interpolation of real/imaginary parts cannot give a good result because of insufficient frequency samples per oscillation period. However, as shown in Figure 4.14 and Figure 4.15, the same interpolation method gives an accurate result for a short microstrip structure.

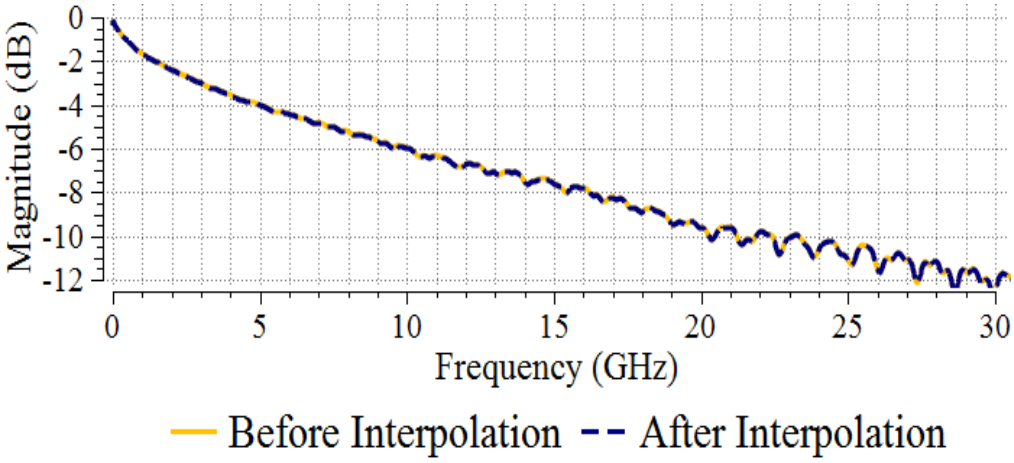

Figure 4.14. Magnitude of SDD21 of the Microstrip before and after Interpolation

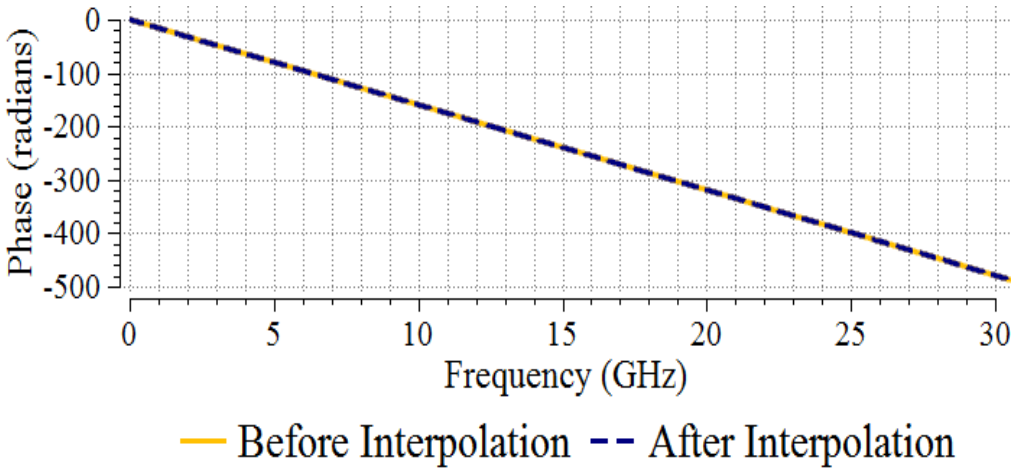

Figure 4.15. Phase of SDD21 of the Microstrip before and after Interpolation

The real and imaginary parts of the short structures do not oscillate as much as the long structures, and so there are enough sample points per oscillation period which results in a more accurate interpolation.

However, the reason for the artifacts appearing in Figure 4.8 and Figure 4.9 is not the magnitude oscillation of the interpolated frequency response shown in Figure 4.12. These artifacts in the time domain will not disappear if the magnitude is corrected with the logarithmic interpolation using the following formula:

$$\log_{10}|\bar{H}_i| = \frac{\bar{\omega}_i - \omega_{k+1}}{\omega_k - \omega_{k+1}} \log_{10}|H_k| + \frac{\bar{\omega}_i - \omega_k}{\omega_{k+1} - \omega_k} \log_{10}|H_{k+1}|, \quad (100)$$

where $\bar{\omega}_i \in [\omega_k, \omega_{k+1}]$. The corrected magnitude of the SDD21 of the 3 m cable interpolated using (100) is shown in Figure 4.16.

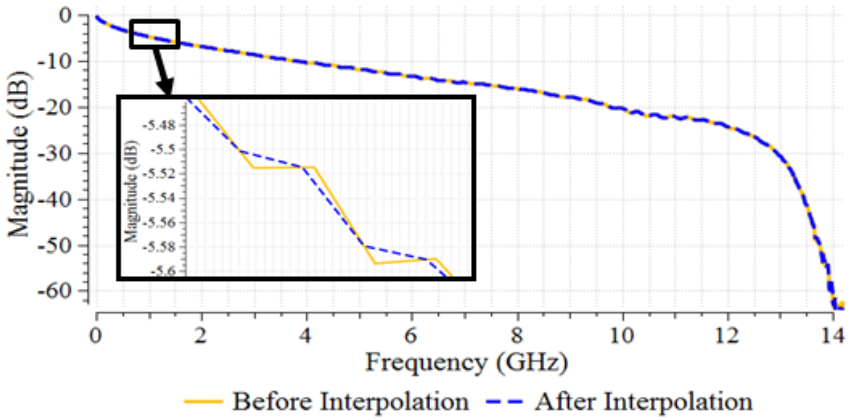

Figure 4.16. SDD21 of th 3 m Cable Using the Corrected Magnitude Interpolation

Magnitude-based interpolation is better than real/imaginary-based interpolation because unlike the latter, magnitudes are generally not oscillated or oscillated at much lower frequencies and the undersampling problem does not manifest itself.

Despite the similarity of the interpolated and the original magintudes shown in Figure 4.16, the time domain artifacts are still present. Figure 4.17 shows the impulse and step responses before and after the interpolation with the corrected magnitude. The difference from interpolation of the real/imaginary parts is that the artificial small copies of the main impulse from both sides have different signs while the signs of the artifacts are the same in case of the interpolation of the real/imaginary parts.

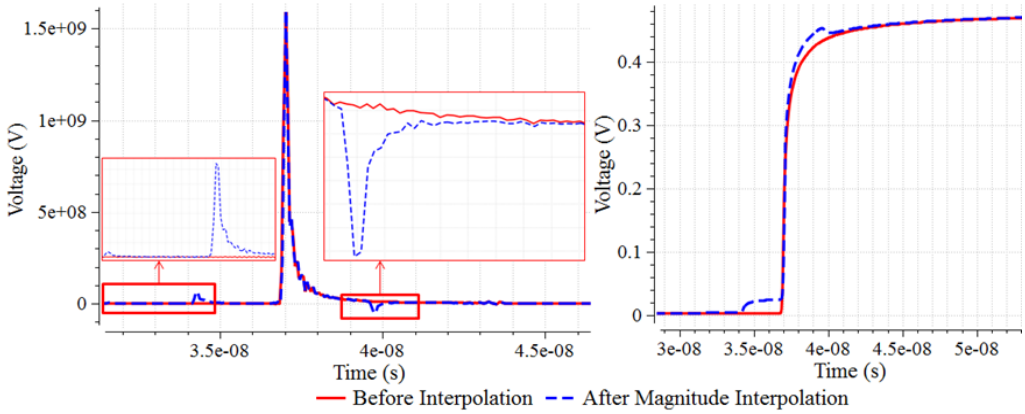

Figure 4.17. Impulse and Step Response of the 3 m cable before and after Magnitude Interpolation

The artifacts seen in Figure 4.17 resemble the aliasing effect in the time domain [1]. Similar to frequency domain aliasing, the effect occurs when the data is undersampled. For undersampled time domain data, the frequency response gets corrupted and, in the same way, the time domain response gets corrupted if the frequency response is undersampled. However, if the step is small enough the aliasing phenomenon does not occur. On the contrary, the artifacts of the inaccurate interpolation appear even if the interpolation step is smaller than the original step for which no artifacts are observed.

To understand the reason behind the artifacts seen in Figure 4.8, Figure 4.9, and Figure 4.17, the nonlinear part of the phase before and after the interpolation should be observed. Extracting the linear part of the transfer function can be done by multiplying the transfer function by $e^{j\omega\tau}$, where τ is a system front delay. This transformation is equivalent to the shift of the time domain impulse response by $-\tau$ [2]. Figure 4.18 shows that the nonlinear part of the phase after interpolation oscillates around the original phase of the 3 m cable. The oscillation amplitude is pretty small, -0.05 radians (less than 3°), but it turns out to be enough to create small copies of the main pulse on both sides of the phase.

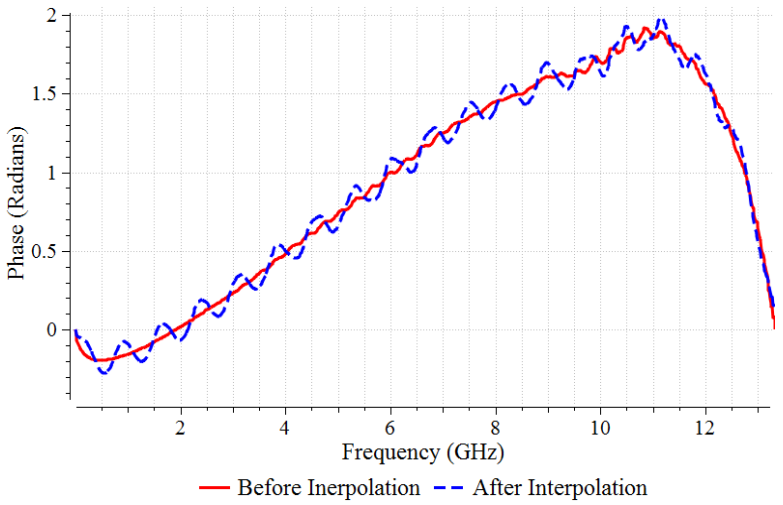

Figure 4.18. Nonlinear Part of the 3 m Cable Phase before and after Interpolation

As shown in [21], the nonlinear part of the phase plays a critical role in the causality property of the transfer function. Thus, the non-causal effects observed in the impulse response after the interpolation are expected. The non-causality in this case is not a reason for the time domain artifacts, but rather both effects are results of the incorrect interpolation.

Figure 4.19, Figure 4.20, and Figure 4.21 illustrate that these artifacts are indeed smaller copies of the original impulse response and they are moving when the interpolation step is changing. The artifacts are close to the main pulse for the 10.2 MHz interpolation step in Figure 4.8. For the 11 MHz interpolation step in Figure 4.19, the distance from the main pulse and artifacts increases on both sides. For the 14.9 MHz interpolation step in Figure 4.20, the left and the right side artifacts are approaching each other and for the 15 MHz interpolation step in Figure 4.21, the left and the right side artifacts meet each other. For real/imaginary interpolation these artifacts have the same sign and are summed, while in the case of magnitude correction, the artifacts have opposite signs and they cancel each other. This phenomenon is periodic and the length of the period is 5 MHz (50% of the original frequency step).

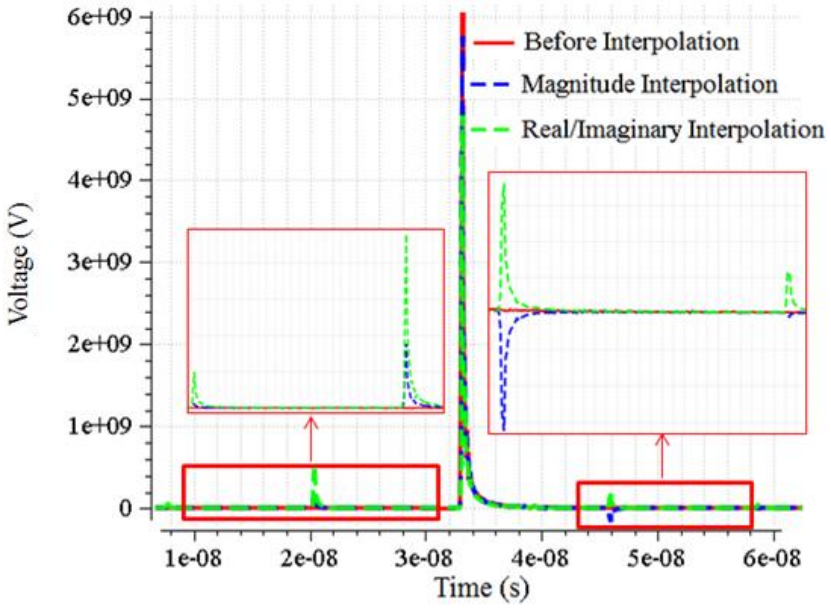

Figure 4.19. Impulse Responses before and after the 11 MHz Step Interpolation

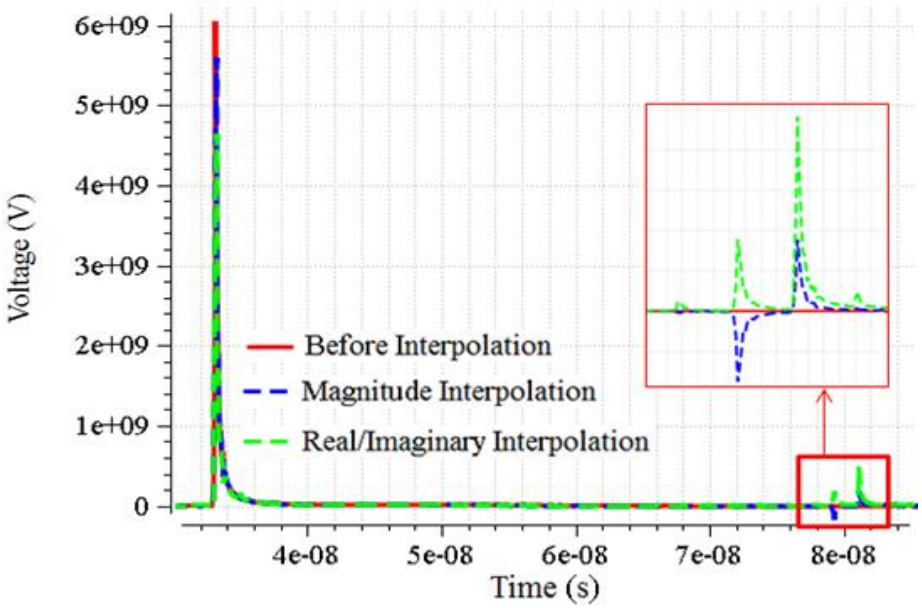

Figure 4.20. Impulse Responses before and after 14.9 MHz Step Interpolation

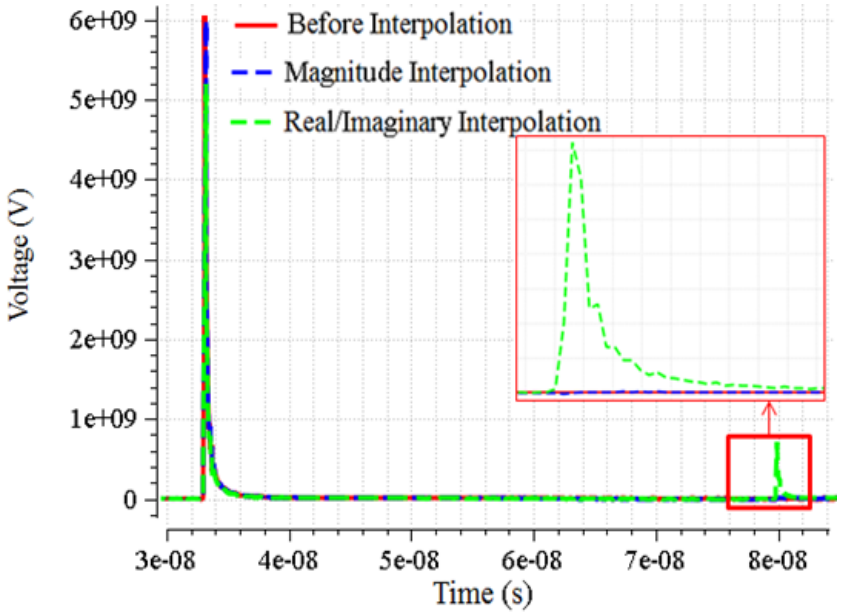

Figure 4.21. Impulse Responses before and after the 15 MHz Step Interpolation

4.2.3. Linear Phase Extraction Technique for Accurate Interpolation. The problem of interpolation shown in Figures 4.15-4.17 exists in the fact that the real and imaginary parts of the 3 m cable are highly oscillated and, in the case of the 10 MHz frequency step, there is an insufficient number of frequency samples per period. The interpolation procedure of this type of data is very sensitive.

In Figure 4.22 there is a given real part of the frequency response of the 3 m cable before and after 10.2 MHz step interpolation (a similar picture takes place for the imaginary part).

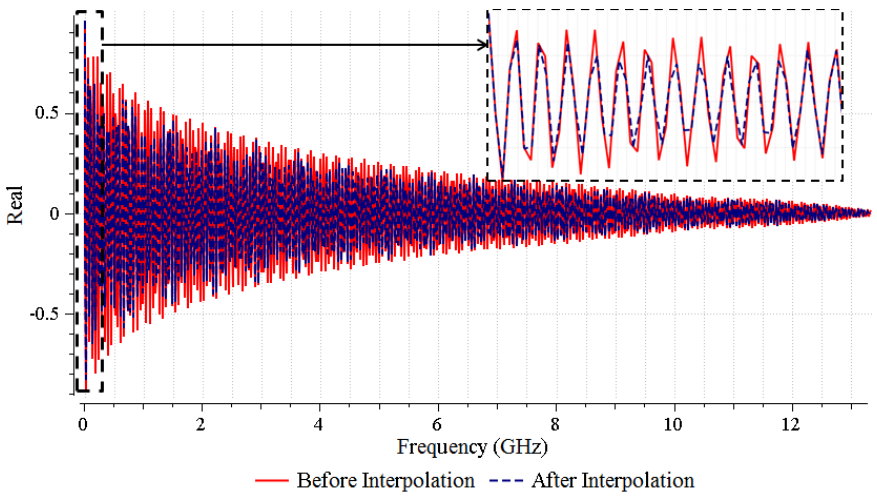

Figure 4.22. Real Parts of the Frequency Response of the 3 m cable before and after 10.2 MHz Frequency Step Interpolation

This problem can be solved if the linear part of the phase before interpolation is removed and then returned after interpolation is done. Figure 4.23 shows that the linear phase extraction before interpolation gives an accurate approximation of the nonlinear part of the phase. Therefore, the obtained impulse and step responses do not have the unwanted artifacts as shown in Figure 4.24 and Figure 4.25.

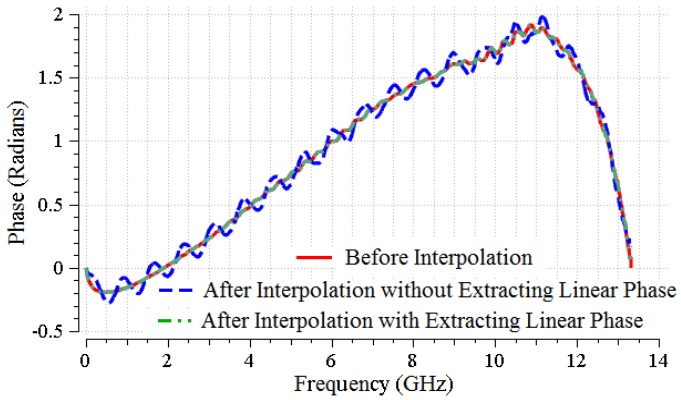

Figure 4.23. Nonlinear Part of the Phase of the Frequency Response of the 3 m Cable Using Interpolation with and without Removing the Linear Part

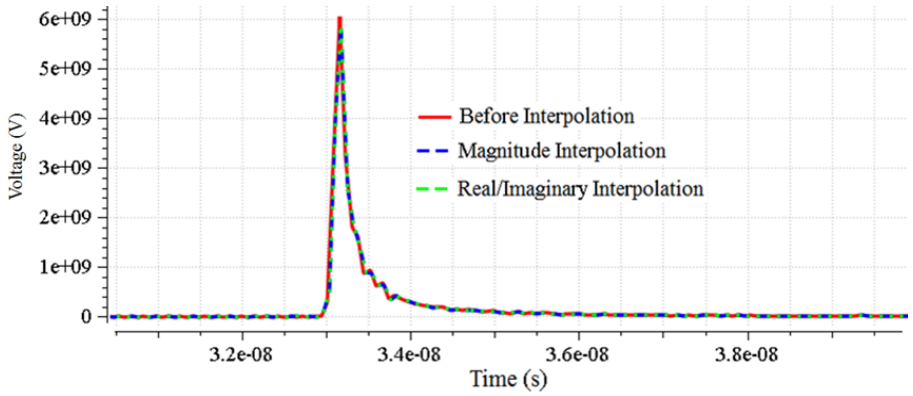

Figure 4.24. Impulse Responses before and after Interpolation Using Linear Phase Extraction before Interpolation

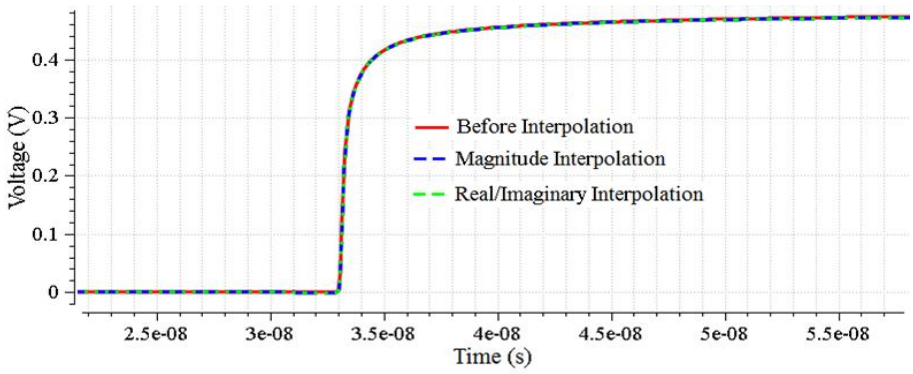

Figure 4.25. Step Responses before and after Interpolation Using Linear Phase Extraction before Interpolation

The interpolation is much more accurate if the linear portion of the phase is removed before interpolation and returned after interpolation because it makes the real/imaginary parts or phase of the transfer function smoother and less oscillated. This method is especially important for electrically long structures.

APPENDIX

DERIVATION OF SQUARE ROOT-BASED CAUSAL EXTRAPOLATION

The following integral has to be calculated:

$$\int_{\omega_N}^{\infty} \frac{\sqrt{\omega}d\omega}{\prod_{q=1}^{N}(\omega-\sigma_q)(\omega-\omega_k)}. \tag{101}$$

Using the substitution $z = \sqrt{\omega}$, the integral above transforms into:

$$\int_{\omega_N}^{\infty} \frac{\sqrt{\omega}d\omega}{\prod_{q=1}^{N}(\omega-\sigma_q)\,(\omega-\omega_k)} = 2\int_{\sqrt{\omega_N}}^{\infty} \frac{z^2 dz}{\prod_{q=1}^{N}(z^2-\sigma_q)\,(z^2-\omega_k)}. \tag{102}$$

Using fractional decomposition:

$$\int_{\sqrt{\omega_N}}^{\infty} \frac{z^2 dz}{\prod_{q=1}^{N}(z^2-\sigma_q)(z^2-\omega_k)} = \left(\sum_{q=1}^{N}\int_{\sqrt{\omega_N}}^{\infty}\frac{\alpha_q dz}{z^2-\sigma_q}\right) + \int_{\sqrt{\omega_N}}^{\infty}\frac{\beta dz}{z^2-\omega_k}. \tag{103}$$

To derive α_q and β, the expression is combined into a common denominator and then for each $z = \sqrt{\sigma_q}$ and $z = \sqrt{\omega_k}$ there is an equation of numerators being equal. The resulting formulas are:

$$\alpha_q = \frac{\sigma_q}{\sigma_q-\omega_k}\left(\prod_{\substack{p=1\\p\neq q}}^{N}(\sigma_q-\sigma_p)\right)^{-1}, \tag{104}$$

and

$$\beta = \omega_k\left(\prod_{p=1}^{N}(\omega_k-\sigma_p)\right)^{-1}. \tag{105}$$

Now, the generic integral $\int_B^{\infty}\frac{dz}{z^2-a}$ has to be solved. The following formula gives the generic solution:

$$\int_B^\infty \frac{dz}{z^2-a} = \frac{1}{2\sqrt{a}} \ln\left|\frac{B+\sqrt{a}}{B-\sqrt{a}}\right|. \tag{106}$$

Using the derived generic integral the following final formula is obtaı

$$\int_{\omega_N}^\infty \frac{\sqrt{\omega}d\omega}{\prod_{q=1}^N(\omega-\sigma_q)(\omega-\omega_k)} = \sum_{q=1}^N \left[\frac{\sqrt{\sigma_q}}{(\sigma_q-\omega_k)\prod_{\substack{p=1\\p\neq q}}^N(\sigma_q-\sigma_p)} \ln\left|\frac{\sqrt{\omega_N}+\sqrt{\sigma_q}}{\sqrt{\omega_N}-\sqrt{\sigma_q}}\right|\right] + \frac{\sqrt{\omega_k}}{\prod_{p=1}^N(\omega_k-\sigma_p)} \ln\left|\frac{\sqrt{\omega_N}+\sqrt{\omega_k}}{\sqrt{\omega_N}-\sqrt{\omega_k}}\right|. \tag{107}$$

Now, the same integral over the negative part of the spectrum has to be calculated:

$$\int_{-\infty}^{-\omega_N} \frac{\sqrt{|\omega|}d\omega}{\prod_{q=1}^N(\omega-\sigma_q)(\omega-\omega_k)}. \tag{108}$$

The following transformation is applied:

$$\int_{-\infty}^{-\omega_N} \frac{\sqrt{|\omega|}d\omega}{\prod_{q=1}^N(\omega-\sigma_q)(\omega-\omega_k)} = (-1)^{N+1} \int_{\omega_N}^\infty \frac{\sqrt{\omega}d\omega}{\prod_{q=1}^N(\omega+\sigma_q)(\omega+\omega_k)}. \tag{109}$$

Derivations equivalent to the positive frequencies case result in the following expression:

$$\int_{\omega_N}^\infty \frac{\sqrt{\omega}d\omega}{\prod_{q=1}^N(\omega+\sigma_q)(\omega+\omega_k)} = 2\left(\sum_{q=1}^N \int_{\sqrt{\omega_N}}^\infty \frac{\gamma_q dz}{z^2+\sigma_q}\right) + 2\int_{\sqrt{\omega_N}}^\infty \frac{\vartheta dz}{z^2+\omega_k}. \tag{110}$$

To derive γ_q and ϑ, the expression is combined into a common denominator and then for each $z = j\sqrt{\sigma_q}$ and $z = j\sqrt{\omega_k}$ there is an equation of numerators being equal. The resulting formulas are:

$$\gamma_q = \frac{-\sigma_q}{-\sigma_q + \omega_k}\left(\prod_{\substack{p=1 \\ p\neq q}}^{N}\left(-\sigma_q + \sigma_p\right)\right)^{-1} = (-1)^{N+1}\alpha_q, \tag{111}$$

and

$$\vartheta = -\omega_k\left(\prod_{p=1}^{N}\left(\sigma_p - \omega_k\right)\right)^{-1} = (-1)^{N+1}\beta. \tag{112}$$

Now, the generic integral $\int_B^{\infty}\frac{dz}{z^2+a}$ has to be solved. The following formula gives the generic solution:

$$\int_B^{\infty}\frac{dz}{z^2+a} = \frac{\pi}{2a} - \frac{1}{a}\arctan\frac{B}{a}. \tag{113}$$

Using the derived generic integral the following final formula is obtained:

$$\int_{-\infty}^{-\omega_N}\frac{\sqrt{|\omega|}d\omega}{\prod_{q=1}^{N}(\omega-\sigma_q)(\omega-\omega_k)} = \sum_{q=1}^{N}\left[\frac{\sqrt{\sigma_q}}{(\sigma_q-\omega_k)\prod_{\substack{p=1 \\ p\neq q}}^{N}(\sigma_q-\sigma_p)}\left(\pi - 2\arctan\sqrt{\frac{\omega_N}{\sigma_q}}\right)\right] + \frac{\sqrt{\omega_k}}{\prod_{p=1}^{N}(\omega_k-\sigma_p)}\left(\pi - 2\arctan\sqrt{\frac{\omega_N}{\omega_k}}\right). \tag{114}$$

Using these derivations, the extrapolation error compensation term can be derived:

$$\begin{aligned} E_k &= \int_{\Omega_{\omega_N}}\frac{\prod_{q=1}^{M_k}\left(\omega_k - \sigma_q^k\right)}{\prod_{q=1}^{M_k}\left(\omega - \sigma_q^k\right)}\frac{\widetilde{U}(\omega)}{\omega_k - \omega}d\omega \\ &= \int_{\Omega_{\omega_N}}\frac{\prod_{q=1}^{M_k}\left(\omega_k - \sigma_q^k\right)}{\prod_{q=1}^{M_k}\left(\omega - \sigma_q^k\right)}\frac{\frac{U(\omega_N)}{\sqrt{\omega_N}}\sqrt{|\omega|}}{\omega_k - \omega}d\omega \\ &= E_k^+ + E_k^-, \end{aligned} \tag{115}$$

$$E_k^+ = \frac{U(\omega_N)}{\sqrt{\omega_N}}\left(\sum_{q=1}^{N}\left[\sqrt{\sigma_q}\prod_{\substack{p=1\\p\neq q}}^{N}\frac{\omega_k-\sigma_p}{\sigma_q-\sigma_p}\ln\left|\frac{\sqrt{\omega_N}+\sqrt{\sigma_q}}{\sqrt{\omega_N}-\sqrt{\sigma_q}}\right|\right]-\sqrt{\omega_k}\ln\left|\frac{\sqrt{\omega_N}+\sqrt{\omega_k}}{\sqrt{\omega_N}-\sqrt{\omega_k}}\right|\right),$$

$$E_k^- = \frac{U(\omega_N)}{\sqrt{\omega_N}}\left(\sum_{q=1}^{N}\left[\sqrt{\sigma_q}\prod_{\substack{p=1\\p\neq q}}^{N}\frac{\omega_k-\sigma_p}{\sigma_q-\sigma_p}\left(\pi-2\arctan\sqrt{\frac{\omega_N}{\sigma_q}}\right)\right]-\sqrt{\omega_k}\left(\pi-2\arctan\sqrt{\frac{\omega_N}{\omega_k}}\right)\right). \quad (117)$$

BIBLIOGRAPHY

[1] A. Oppenheim, A. Willsky and I. Young, Signals and systems, Prentice-Hall International, 1983.

[2] A. Papoulis, The Fourier integral and its applications, McGraw-Hill electronic sciences series, 1962.

[3] D. M. Pozar, Microwave Engineering, 4 edition, Wiley, 2012.

[4] P. Triverio, S. Grivet-Talocia, M. Nakhla, F. Canavero and R. Achar, "Stability, Causality, and Passivity in Electrical Interconnects Models," *IEEE Trans. on Advanced Packaging*, vol. 30, no. 4, pp. 795-808, 2007.

[5] Y. Shlepnev, "Quality of S-parameter models," in *Asian IBIS Summit*, Yokohama, 2011.

[6] B. Gustavsen and A. Semlyen, "Enforcing passivity for admittance matrices approximated by rational functions," *IEEE Trans. Power Systems*, vol. 16, no. 1, pp. 97-104, 2001.

[7] E. Campbell, A. Morales and S. Agili, "A simple method for restoring passivity in S-parameters using singular value decomposition," in *Consumer Electronics (ICCE), 2010 Digest of Technical Papers International Conference on*, 2010.

[8] D. Saraswat, R. Achar and M. Nakhla, "Restoration of passivity in S-parameter data of microwave measurements," in *Microwave Symposium Digest, 2005 IEEE MTT-S International*, 2005.

[9] J. Bilmes, "EE518 DSP - University of Washington, EE," 2001. [Online]. Available: http://melodi.ee.washington.edu/courses/ee518/notes/.

[10] N. Nussenzveig, Causality and dispersion relation, Academic Press, 1972.

[11] P. Triverio and S. Grivet-Talocia, "A robust causality verification tool for tabulated frequency data," in *Signal Propagation on Interconnects, IEEE Workshop on*, 9-12 May 2006.

[12] P. Perry and T. Brazil, "Hilbert-transform-derived relative group delay measurement of frequency conversion systems," in *Microwave Symposium Digest, 1996., IEEE MTT-S International*, 1996.

[13] E. Song, J. Cho, J. Kim and D. G. Kam, "Causality enforcement in Transient Simulation of HDMI Interconnects with Magnitude Equalization," in *IEEE International Symposium, EMC*, 2007.

[14] C. Yoon, M. Tsiklauri, M. Zvonkin, J. Fan, L. Drewniak, A. Razmadze, A. Aflaki, J. Kim and Q. Chen.

[15] B. Gustavsen and A. Semlyen, "Rational approximation of frequency domain responses by vector fitting," *Power Delivery, IEEE Transactions on*, vol. 14, no. 3, pp. 1052-1061, July 1999.

[16] W. Janke and G. Blakiewicz, "Semi-analytical recursive algorithms for convolution calculations," *Circuits, Devices and Systems, IEEE Proceedings*, vol. 142, no. 2, pp. 125-130, 1995.

[17] EMS-PLUS, *Fast ElectroMagnetic Analysis Suite (FEMAS)*, 2010-2015.

[18] A. Ferrero and S. Salicone, "A fast frequency-domain interpolation method for the evaluation of the frequency and amplitude of spectral components," in *Instrumentation and Measurement Technology Conference (I2MTC), IEEE*, 3-6 May 2010.

[19] T. Grandke, "Interpolation algorithms for discrete fourier transforms of weighted signals," *IEEE Trans. Instr. Meas*, Vols. IM-32, no. 2, pp. 350-355, June 1983.

[20] A. Ferrero and G. D'Antona, Digital Signal Processing for Measurement Systems. Theory and Applications, New York, NY, USA: Springer series on: Information Technology: Transmission, Processing, and Storage, 2006.

[21] M. Tsiklauri, M. Zvonkin, J. Fan, J. L. Drewniak, Q. B. Chen and A. Razmadze, "Causality and Delay and Physics in Real Systems," in *IEEE International EMC Symposium*, Raleigh, NC, 2014.

[22] P. Triverio, "Robust Causality Check for Sampled Scattering Parameters via a Filtered Fourier Transform," *Microwave and Wireless Components Letters, IEEE*, vol. 24, no. 2, pp. 72-74, Feb 2014.

[23] K. N. Van Dalen, E. Slob and C. Schoemaker, "Generalized minimum-phase relations for memory functions associated with wave phenomena," *Geophysical Journal International*, vol. 195, no. 3, pp. 1620-1629, 2013.

VITA

Mikhail Zvonkin was born on March 20, 1990 in Moscow, Russian Federation. He received the degree of Specialist in Mathematics (equivalent to Master of Science) from Moscow State University, Moscow, Russia, at the School of Mechanics and Mathematics, Department of Mathematical Logic and Theory of Algorithms in July 2012. He received the degree of Master of Science in Electrical Engineering from Missouri University of Science and Technology, Rolla, Missouri, USA, at the Department of Electrical and Computer Engineering in December 2015.